Publications of the Astronomical Society of Australia (2026), **43**, e120, 23 pages
doi:10.1017/pasa.2026.10245

CAMBRIDGE UNIVERSITY PRESS

Research Article

The MWA Interestingly Deep AStrophysical (MIDAS) survey: Survey description and first data release

Sean Paterson[1], Nicholas Seymour[1], Natasha Hurley-Walker[1], Timothy James Galvin[2], Stefan Duchesne[2], John Morgan[2] and Thomas Franzen[3]

[1]International Centre for Radio Astronomy Research, Curtin University, Bentley, WA, Australia, [2]CSIRO Space and Astronomy, Commonwealth Scientific and Industrial Research Organisation, Bentley, WA, Australia and [3]SKA Observatory, Jodrell Bank, Lower Withington, Macclesfield, UK

Abstract

We present the deepest Murchison Widefield Array (MWA) survey to date, targeting the GAMA9 and GAMA23 survey fields at 215.68 MHz. With a bandwidth of 30.72 MHz, the two images cover ∼1 250 deg^2 for the GAMA9 field and ∼850 deg^2 for the GAMA23 field, with an angular resolution of ∼60″. The GAMA9 image was formed from 1 282 2-min snapshot observations (42.7 h) and the GAMA23 image from 1 701 observations (56.7 h) achieving depths of 0.923 ± 0.003 and 0.331 ± 0.001 mJy/beam at the field centres, respectively. We processed the data with an updated version of the GLEAM-X pipeline tuned for deep surveys and make this MWA `Deep Imaging Pipeline` code public. Updates to the pipeline include automation of the observation downloading, calibration, and imaging along with optimisation of the `CLEAN`ing methods and parameters. Above 5σ, we catalogue 53 419 and 80 407 radio components in the GAMA9 and GAMA23 fields, respectively. We find that the completeness corrected source counts for both fields are in good agreement down to 25–50 mJy with those from LOFAR and earlier MWA surveys. We demonstrate the utility of this survey by highlighting a few sources of particular interest and describing future science possible with this survey.

Keywords: Techniques: interferometric; radio continuum: general; catalogues; surveys; galaxies: general

(Received 24 April 2025 UTC; revised 21 July 2026 UTC; accepted 28 July 2026 UTC)

1. Introduction

The low-frequency radio sky has become a new frontier over the last decade with numerous observations from facilities such as the LOw-Frequency ARray (LOFAR; Van Haarlem et al. 2013), the Murchison Widefield Array (MWA; Tingay et al. 2013) and the upgraded Giant Metrewave Radio Telescope (uGMRT; Gupta et al. 2017). At lower radio frequencies, emissions evolve on relatively long time scales (Franzen et al. 2021), assisting in the study of remnant radio galaxies (Quici et al. 2021), galaxy cluster relics and halos (George et al. 2015, 2017), supernova remnants (Mantovanini et al. 2024), and many other phenomena. Emissions at these frequencies originate from the lobes of active galactic nuclei (AGN), rather than the core; this negates beaming effects and local interactions (Franzen et al. 2021), enabling reliable measurements for average jet powers. In addition, well-calibrated low-frequency radio data offers extinction-free methods to evaluate star formation rates (Beswick et al. 2015; Heesen et al. 2019).

The study of the universe at lower radio frequencies continues to advance with the Square Kilometre Array Observatory's (SKAO)[a] Low telescope under construction, and thanks to pathfinders such as LOFAR and precursors such as the MWA currently in operation, a greater number of low-frequency radio surveys are being conducted. The LOFAR Two-metre Sky Survey (LoTSS; Shimwell et al. 2017, 2019, 2022) is an ongoing survey of the northern sky in the 120–168 MHz range. At the time of writing, the second data release covers 27% of the northern sky over two regions with areas of 4 178 deg^2 and 1 457 deg^2, respectively (Shimwell et al. 2022). The resulting Stokes I image achieves a median root mean squared error (RMS) of 83 μJy/beam with a resolution of 6″. From this they have produced a catalogue containing 4 396 228 radio sources.

For the southern sky, the GaLactic and Extragalactic All-sky MWA (GLEAM; Wayth et al. 2015) survey produced a catalogue of 307 455 radio sources over a 24 831 deg^2 area in the frequency range 72–231 MHz (Hurley-Walker et al. 2017) using observations conducted with the MWA in its Phase I configuration. This catalogue was extended with a second GLEAM data release producing a compact source catalogue of 22 037 components for an area that covered ∼50% of the Galactic plane (Hurley-Walker et al. 2019). The MWA was then upgraded moving it to 'Phase II' with the 'extended' configuration which offered increased sensitivity and a higher angular resolution with longer baselines and improvements in their distribution (Wayth et al. 2018), With this configuration the GaLactic and Extragalactic All-sky MWA eXtended (GLEAM-X; Hurley-Walker et al. 2022) survey observed the sky south of Dec +30° across a frequency range of 72–231 MHz; the initial data release over an area of 1 447 deg^2 produced a catalogue of 78 967 sources. The second

Corresponding author: Sean Paterson; Email: sean.paterson@icrar.org

Cite this article: Paterson S, Seymour N, Hurley-Walker N, Galvin TJ, Duchesne S, Morgan J and Franzen T. (2026) The MWA Interestingly Deep AStrophysical (MIDAS) survey: Survey description and first data release. *Publications of the Astronomical Society of Australia* **43**, e120, 1–23. https://doi.org/10.1017/pasa.2026.10245

[a]https://www.skao.int/en.

© The Author(s), 2026. Published by Cambridge University Press on behalf of Astronomical Society of Australia. This is an Open Access article, distributed under the terms of the Creative Commons Attribution licence (https://creativecommons.org/licenses/by/4.0/), which permits unrestricted re-use, distribution and reproduction, provided the original article is properly cited.

GLEAM-X data release provides a catalogue of an additional 624 866 radio sources from a processed area of 12 892 deg^2 (Ross et al. 2024). Most recently, a third GLEAM-X data release utlised a joint deconvultion technique to combine GLEAM and GLEAM-X data for an area covering ∼3 800 deg^2 of the southern Galactic Plane, delivering improved fidelity with a resulting source catalogue containing 98 207 radio sources (Mantovanini et al. 2025).

The Galaxy and Mass Assembly (GAMA) project was designed to study galaxy structures for low to intermediate redshift galaxies and evaluate the cold dark matter (CDM) model (Driver et al. 2009). It has two components, a spectroscopic survey and a compilation of imaging with photometry across the electromagnetic spectrum. Liske et al. (2015) reported an observational campaign using the Anglo-Australian Telescope for a ∼286 deg^2 area across five regions collecting spectra with the AAOmega spectrograph. These spectra cover the wavelength range 3 740–8 850 Å with a pixel size of 1.04 Å. The spectroscopic survey was expanded further by Driver et al. (2022) using publicly available data derived from *GALEX*, ESO KiDS, ESO VIKING, *WISE*, and *Herschel* Space Observatory imaging for a slightly reduced area of ∼250 deg^2 across the five regions. The resultant survey offers a wealth of data including, but not limited to, galaxy spectra, spectroscopic redshifts and stellar masses. It covers frequency ranges from X-ray (1 nm) to microwave (1 m) and at the time of writing has resulted in spectra for 248 682 galaxies and 330 542 redshifts with a redshift completeness of 95% to $r_{\rm KiDS} = 19.65$ mag.

Recently, the Evolutionary Map of the Universe (EMU; Norris et al. 2021, Hopkins et al. 2025) project has extended the data available for the 60 deg^2 GAMA23 region into the radio band with observations at 888, 936 and 1 320 MHz (Leahy et al. 2019; Gürkan et al. 2022) produced with the Australian SKA Pathfinder (ASKAP; Johnston et al. 2007, DeBoer et al. 2009, Hotan et al. 2021) telescope, a pathfinder to the SKAO's Mid telescope. EMU will ultimately cover the entire Southern sky at dec< 0 deg including the other four GAMA fields. In addition, a wealth of derived products have been determined from the surveys including, but not limited to, stellar mass (Driver et al. 2022) and AGN bolometric luminosities (Thorne et al. 2021). The introduction of low-frequency radio data with a greater sensitivity to these fields that are already well studied at higher frequencies opens up further opportunities to better understand the physical processes occurring within them.

The MWA Interestingly Deep AStrophysical (MIDAS) survey offers complementary data to GLEAM-X for selected GAMA regions. GLEAM-X provides low-frequency radio data for a wide-field view of the southern hemisphere, here we offer additional depth at 215.68 MHz to the GAMA9 and GAMA23 regions through a concentrated observation strategy with ∼70–90 h of integration per field.

We provide an outline of the MWA observations conducted for the MIDAS survey that were processed for this data release in Section 2. In Section 3, we describe the pipeline and automation used to process the observational data. The observation selection and mosaicking process is described in Section 4. Then in Section 5 we outline the properties of the final images and the resulting data products along with a preliminary investigation into a few example sources exhibiting atypical radio emission to demonstrate the utility of the survey. Lastly, in Section 6 we summarise the results.

Table 1. Description of the GAMA fields observed where the first row is the range of the RA for the observed GAMA field in degrees, the second row is the range of Dec for the field in degrees and the third is the area of region in square-degrees. The fourth row is the MWA project ID the observations were made under, the fifth is the dates the observational campaign started and the sixth is the date the campaign finished. The seventh row is the range of RA for the pointing centre of the observations in degree, the eighth row is Dec for the observation centres and the ninth is the approximate range for the areas observed (per observation). The tenth row is the average RMS in each snapshot measured by `BANE` after processing through the pipeline outlined in Section 3. The eleventh is the total number of observations conducted and the twelfth is the number of observations that were used for the final mosaics.

	Region	
	GAMA23	GAMA9
RA range (deg)	339 to 351	129 to 141
Dec range (deg)	−35 to −30	−2 to 3
Area of GAMA field (deg^2)	60	60
Project ID	G0047	G0069
Observing start date	March 2018	April 2020
Observing end date	August 2018	September 2020
Observing RA centre (deg)	335.7 to 354.3	124.1 to 146.6
Observing Dec centre (deg)	−40.3 to −26.8	−11.1 to 11.9
Observing area per pointing (deg^2)	∼700–750	∼600–700
Average snapshot RMS (mJy/beam)	6	17
Total observations	2 136	2 657
Observations mosaicked	1 701	1 282

2. Observational data

To add to the wealth of information available from the GAMA project, we used the MWA radio telescope to conduct thousands of observations of the five GAMA fields along with the Spitzer South Pole Telescope Deep Field. The observations were carried out over the same frequency range as GLEAM to offer complementary data to the GLEAM(-X) surveys (Beardsley et al. 2019). They were conducted in 2-min snapshots due to the fixed grid of points at which the MWA can form beams, i.e. it cannot track sources. This strategy also adds the benefit of being able to apply a non-varying beam pattern and ionospheric correction to each snapshot rather than multiple corrections that would be required for longer-duration observations. We used MWA's 'Phase II extended' configuration as it maximises the angular resolution while minimising classical and sidelobe confusion. For a subset of day time observations, the survey made use of a Sun nulling technique that places the Sun in a low-sensitivity area between the sidelobes.

We focused our deep field imaging on two of the most observed fields from the GAMA survey, GAMA9 and GAMA23. From the surveys, we selected observations centred at 215.68 MHz with a bandwidth of 30.72 MHz outlined in Table 1. This frequency offers a generous field of view and the addition of 215.68 MHz data for these fields will complement the existing data, enabling more science opportunities.

Under the MWA project ID G0047 during the period March–August 2018, 2 136 observations (71.2 h) were conducted of the GAMA23 field. Despite the wide field of view of the MWA

https://doi.org/10.1017/pasa.2026.10245 Published online by Cambridge University Press

(>600 deg^2), the main focus of these observations was the 60 deg^2 of multi-wavelength and spectroscopic data between RA +339° to +351° and between Dec −35° to −30°. This field is close to zenith for the MWA with very few bright sources in the field of view, providing ideal conditions for observing.

The second selected field, GAMA9, is off-zenith with numerous bright sources in the field of view, including Hydra-A. This presented significant challenges for imaging discussed in Section 3.2. These observations focused on the 60 deg^2 area from RA +129° to +141° and Dec −2° to +3°. The survey observed this field between April 2020 and September 2020 under MWA project ID G0069, producing 2 657 observations (88.6 h).

3. Deep imaging pipeline

To process the thousands of observations required for the deep field images, we created the `Deep Imaging Pipeline (DIP)`.[b] `DIP` is adapted from the pipeline used in the GLEAM-X survey[c] and utilises a combination of Nextflow (Di Tommaso et al. 2017), Python and Bash scripts to automatically download the data from the All-Sky Virtual Observatory (ASVO)[d] and then process it. The pipeline is primarily designed to process MWA data on the Setonix supercomputer node at the Pawsey Supercomputing Centre,[e] however it can easily be ported to other high performance computing environments and is fully customisable allowing any selection of `CLEANing`[f] parameters with minor modification. The pipeline takes a list of MWA observation IDs and outputs a `CLEANed` image, RMS map, background map and source catalogue for each observation.

For this work, we used resources provided by the Pawsey Supercomputing Centre, including the Garrawarla and Setonix supercomputer nodes, processing ∼120 observations per day and Acacia, a distributed disk-array, for storage. The processing is broken down into three main steps; calibration, imaging, and post-imaging. We describe these steps below, highlighting the modifications to the GLEAM-X pipeline.

While all the individual two-minute snapshot observations used here pointed at the GAMA fields in question, they all had different off-zenith electrically steered beams and different sky pointing centres. Hence, the data could not be combined in the (u, v)-plane or imaged in one go as the joint-deconvolution algorithms (Van Der Tol et al. 2018) do not scale easily past ∼20 observations (Mantovanini et al. 2025). Hence, each snapshot observation was imaged and CLEANed separately.

3.1. Calibration

Calibration was performed using the same methods as GLEAM-X. We utilised the GLEAM Global Sky Model (GGSM) from the GLEAM-X pipeline that was derived primarily from GLEAM along with additional models for the brighter and more complex sources from literature (Hurley-Walker et al. 2022; Ross et al. 2024). This model provides the flux densities for the observed sources from which we derive our per-frequency channel, per-polarisation, per-antenna bandpass calibration solutions.

For each observation, the model was cropped to the 250 brightest sources after applying an estimate of the primary beam attenuation predicted by the Full Embedded Element (FEE; Sokolowski et al. 2017) response within a radius of 30° from the pointing centre. `MitchCal` (Offringa et al. 2016) was then used to generate the calibration solution for each measurement set.

A phase slope was generated for the solution by dividing through by a selected reference antenna, the last tile in the array, number 128. The phase slope per polarisation for each MWA station calibration solution was inspected.[g] A linear trend was fitted; if the RMS of the residual was >20%, the entire station was automatically flagged for the remainder of the observing night. If one or more tiles were flagged, a new calibration solution was generated. If more than 50 bad tiles were detected, the processing was terminated and the observation was flagged as unsuccessful. A total of 131 observations were flagged unsuccessful in GAMA23 and 179 observations in GAMA9.

Additionally, if more than 25% of the solutions were flagged due to radio-frequency interference (RFI), failure to converge, or unmodelled sources in the sidelobes), the processing was halted and the observation was flagged as unsuccessful. This criteria did not flag any observations in GAMA23, but flagged an additional 22 observations in GAMA9. Once all quality checks were passed, the calibration solution was applied to the measurement set.

During the ASVO download, potential RFI is flagged; for the final calibration step we rerun the RFI flagging by calculating the running mean and standard deviation for the (u, v)-distance vs amplitude for the visibilities. If there were data points that were 3σ above the computed running mean, the baselines were flagged completely.

3.2. Imaging

The imaging was performed with WSCLEAN utilising a similar method to the GLEAM-X pipeline, except refining arguments to reduce the RMS noise and improve deep imaging results. For the `CLEANing`, we moved from the w-stacking method used in GLEAM-X to w-gridding. Rather than assigning visibilities to the nearest w-plane, this method grids them to a small range of weighted w-planes (Offringa et al. 2014; Arras et al. 2021; Ye et al. 2022), significantly improving the data reduction speed with no penalty to image fidelity. We then followed the GLEAM-X method and imaged four separate sub-bands, each with a bandwidth of 7.68 MHz and `CLEANed` the full integrated 30.72 MHz wide band image. However, as our focus was on the final wideband image, we did not implement spectral fitting on the sub-bands that would enforce smooth spectra.

As observations move off-zenith, the shape of the primary beams differ for each polarisation. The further a pointing is from zenith, the greater the difference in response from the different dipole orientations, and therefore the greater the intrinsic polarisation of the primary beam. With the varying elevation of the fields, different pointings were required which resulted in different primary beam shapes. Therefore, we followed a similar method as the original GLEAM survey (Hurley-Walker et al. 2017)

[b] https://github.com/sjpaterson/dip.
[c] https://github.com/GLEAM-X/GLEAM-X-pipeline.
[d] https://asvo.mwatelescope.org.
[e] https://pawsey.org.au.
[f] Imaging was completed with WSCLEAN (Offringa et al. 2014; Offringa & Smirnov 2017) detailed in Section 3.2.
[g] Using a modified version of https://github.com/MWATelescope/mwa-calplots to automatically detect potentially problematic tiles available at https://github.com/sjpaterson/mwa-calplots.

https://doi.org/10.1017/pasa.2026.10245 Published online by Cambridge University Press

and imaged the XX and YY linear polarisations separately. We used the `link-polarizations` option to ensure that any component detected in either polarisation was CLEANed in both and applied the primary beam to form a pseudo-Stokes *I* image in the post-imaging stage (Section 3.3).

3.2.1. Noise reduction

In the final deep image, there are expected to be three main sources of noise: thermal, sidelobe and confusion. The thermal noise for the MWA is dominated by the sky noise with a small contribution from the receiver, while the sidelobe noise is additional noise introduced from the synthesised beam's sidelobes of residual unCLEANed sources, both faint sources in the primary beam and potentially brighter sources in the grating lobes of the telescope (Franzen et al. 2016). The confusion noise is the fluctuations in the image caused by the collective contribution of all sources within the main lobe of the synthesised beam where, as the number of observations stacked increases, the number of sources observed increases until the classical confusion limit is reached and the density of the sources become so great that they cannot be resolved (Condon 1974; Franzen et al. 2016).

As confusion and sidelobe noise were expected to dominate the final mosaicked images, we selected a uniform weighting scheme. Uniform weighting provides a smaller beam minimising confusion noise and a more Gaussian main lobe response minimising sidelobe noise. These advantages are partly offset by a higher thermal noise due to the down-weighting of short baselines.

To further reduce sidelobe noise, a cosine-weighted window (Tukey) function (Harris 1978) was applied to the inner (u, v)-plane to smooth out the sensitivity at short baselines to minimise 'pedestals' in the dirty beam. We found that an inner Tukey window of 0λ to 875λ offered a good trade-off between sensitivity and rejection of large-scale structure.

3.2.2. Robust clean masking

A full run of DIP was initially run on the GAMA9 and GAMA23 fields using an `auto-mask` threshold of 3σ. The resulting outputs were the CLEANed images, RMS maps produced by BANE (Hancock et al. 2012, 2018) and source catalogues produced by AEGEAN[h] (Hancock et al. 2012, 2018) for each snapshot. Using this level of `auto-mask` cleans the image well, but as a side effect it deconvolves noise peaks removing flux from real sources as described by Duchesne et al. (2025a, Appendix A.2.).[i] These errors accumulate when stacking snapshots resulting in a large flux density offset for all detected sources when compared to the reference catalogue. To prevent this from occurring, DIP was rerun using a CLEANing mask (`fits-mask`) to attempt to clean only real sources.

To generate the mask, we created mosaics from the the 3σ auto-mask CLEANed snapshots and then performed blind source finding on them with AEGEAN. While the flux densities in the source catalogues are incorrect, the sources detected and their positions are real.

We utilised the auto-masked CLEANed snapshots and RMS maps, selecting all pixels above 3σ and creating island maps. We then referenced the source positions in the catalogue produced from the mosaic and removed any island that did not have a corresponding source associated to it. The final reduced island maps were then used for the `fits-mask` parameter during the re-processing of the snapshots.

3.2.3. Other imaging parameters

Through the use of the `wgridder` option in WSCLEAN, we found an approximate 2.5× speed increase over the *w*-stacking method. This speed improvement made available additional CPU cycles to fine-tune the imaging options and further improve the CLEANing process. We investigated altering the number of sub-bands imaged, the auto-threshold limit, the multi-scale gain, the maximum number of major CLEANing iterations (`nmiter`), the peak flux density reduction per iteration (major iteration gain referred to as `mgain`) and the image size.

To gauge the behaviour of the selected parameters for our visibilities, we CLEANed a small number of observations from GAMA9 using a number of different parameter combinations. A collection of ten observations that represented different imaging conditions were used to provide a consistent comparison through this parameter fine-tuning process. Altering the multi-scale gain from 0.05 to 0.25 did not result in a significant change in the image RMS. Variations of `mgain` between 0.6 and 0.95 along with `nmiter` between 5 and 20 revealed an optimal reduction of the image RMS for a minimal increase in computational time with an `mgain` value of 0.75 and a `nmiter` value of 10. The `mgain` change resulted in a decrease of RMS by 2–5% without any significant change in compute time (less than a minute), while the `nmiter` change saw a 10% improvement in RMS with an extra ∼60 min compute time. Increasing the number of sub-bands from 4 to 8 and 16 resulted in a reduction in the image RMS by 2–6% but required a 60–150 min increase in processing time. Increasing the image size while maintaining the pixel scale CLEANed a larger area that resulted in an image RMS reduction with a small increase in processing time. Although some parameters increase storage requirements, we had sufficient resources to meet those requirements. Therefore, for our final parameter values we chose to decrease the `mgain` from 0.85 used in the GLEAM-X pipeline to 0.75, increased `nmiter` from 5 to 10 and increased the image size from 8 000 pixels × 8 000 pixels to 10 000 pixels × 10 000 pixels.

As a result, the WSCLEAN parameters listed in Table 2 including a comparison with GLEAM-X, were selected for the image reduction process.

3.3. Post imaging

CLEANing resulted in images of the XX and YY polarisations with angular resolutions of ∼1′. The Stokes *I* (I_I) image was formed using the methods implemented by Sault et al. (1996) and Morgan et al. (2022) with

$$I_I(l) = \frac{\sum_p A(p)B(l,p)I(l,p)/\sigma^2(p)}{\sum_p A^2(p)B^2(l,p)/\sigma^2(p)}, \quad (1)$$

where p is the linear polarisation (XX and YY), $A(p)$ is a direction-independent scaling correction, $B(l, p)$ is the sky direction and polarisation-dependent primary beam power pattern, $I(l, p)$ is the intensity of each polarisation and σ is the RMS at the centre of the

[h]Throughout this article, source finding was performed using the default settings for AEGEAN which can be obtained from https://github.com/PaulHancock/Aegean.

[i]Similar tests were performed for MIDAS data and showed similar results, with further tests verifying that the FITS masking approach reduced the issue.

https://doi.org/10.1017/pasa.2026.10245 Published online by Cambridge University Press

Table 2. Comparison of the parameters used for WSCLEAN between GLEAM-X and DIP. The first column is the parameter, the second column is the values used in GLEAM-X and third column is the values used in DIP. The 'scale' parameter is dependant on the central frequency of the observations; here we provide the value used for the processing on channel 169 (215.68 MHz). These are the parameters used for imaging the snapshots that are mosaicked for the final deep field images with the fits-mask input described in detail in Section 3.2.2.

Parameter	GLEAM-X	DIP
`wgridder`	No	Yes
`multiscale`	Yes	Yes
`mgain`	0.85	0.75
`multiscale-gain`	0.15	0.15
`nmiter`	5	10
`niter`	10000000	10000000
`auto-mask`	3	Not used
`fits-mask`	Not used	Yes
`auto-threshold`	1	1
`size`	8000 8000	10000 10000
`scale`	0.0035503	0.0035503
`weight`	Briggs 0.5	Uniform
`taper-inner-tukey`	Not used	875
`minuv-l`	Not used	0
`pol`	I	XX,YY
`link-polarizations`	No	Yes
`fit-spectral-pol`	2	Not used
`reuse-primary-beam`	Yes	No
`apply-primary-beam`	Yes	No
`join-channels`	Yes	Yes
`channels-out`	4	4

beam for the primary beam corrected polarisation image, which like the scaling correction is assumed to be direction-independent.

The primary beam power for the XX and YY polarisations were calculated using the `mwa_pb_lookup` package[j] (Morgan & Galvin 2021), which utilises the beam model created by Sokolowski et al. (2017). This software generates a beam intensity image based on the imaged polarisations providing a one-to-one pixel map for the beam power ($B(l, p)$).

The beam intensity images were applied to each linear polarisation to correct for the primary beam and `BANE` was run to estimate the RMS. The beam intensities were used to determine the location of peak sensitivity and the RMS value (σ) at this location for each polarisation was recorded. To determine the scaling factor $A(p)$, we performed a blind source search on each primary beam corrected polarisation image using the source finding software `AEGEAN`. To ensure that the most reliable sources were selected, the source catalogues were reduced to isolated sources that did not have a neighbour within a 6′ cross-matching radius, had a flux density > 0.5 Jy, and were matched to a source in the GGSM sparse unresolved catalogue with a maximum separation distance to the catalogue source of 1′. The integrated flux density ratios between the filtered sources in each polarisation and the corresponding sources in the GGSM catalogue were calculated. The weighted average integrated flux density ratio was calculated for each linear polarisation using the signal-to-noise ratio (SNR) of the MIDAS sources, down-weighting sources with lower SNRs. This resulted in an average scaling factor ($A(p)$) of 0.91 ± 0.11 for GAMA9 and 1.07 ± 0.02 for GAMA23.

The Stokes I image was formed using Equation (1), the RMS and background was estimated with `BANE` and a source catalogue was produced by `AEGEAN`. A quality check for a minimum of 500 sources was applied; any observation that did not pass this check was rejected. To correct source position offsets introduced in the snapshot images due to ionospheric distortions, we utilised `FITS_WARP`[k] which calculates the source position offsets between the observational source catalogue and a reference catalogue with accurate source locations, fits a general non-parametric model to the vector offsets using a radial basis function and then applies a de-distortion correction to the observation in the image plane (Hurley-Walker & Hancock 2018). Before `FITS_WARP` received the observation source catalogue, it was reduced to isolated sources that did not have a neighbouring source within 6′ to avoid source confusion during the matching process. For the reference catalogue, we utilised the positional-based catalogue of unresolved sources generated from the NRAO VLA Sky Survey (NVSS; Condon et al. 1998) and the Sydney University Molonglo Sky Survey (SUMSS; Bock et al. 1999; Mauch et al. 2003; Murphy et al. 2007) described in detail by Hurley-Walker et al. (2022).

Previous flux scaling corrections apply a single multiplicative factor to the entire image. To determine and correct systematic spatial flux density scale errors we utilise `flux_warp`[l] (Duchesne et al. 2020), parsing a new source catalogue generated with `AEGEAN` along with the GGSM sparse unresolved catalogue. This detects the differences in source flux density between the catalogues and corrects the image using a user selectable mode. We selected the quadratic screen mode because it provided a good fit to our data while providing a robustness to outliers. This screen fits a two-dimensional second order polynomial model to the differences in the flux density scale differences and applies a correction. The resulting corrected output image was the final image considered for use in the deep field mosaic. From this final image, the final RMS and catalogue were produced with `BANE` and `AEGEAN`, respectively.

3.4. Final quality control

In the initial processing run, if an observation fails, often due to random compute/disk errors, it is reattempted for a maximum of three attempts without change. However, after the initial processing run, a second run was initiated for all observations that failed the initial three attempts. The second run used a different reference tile for the calibration outlined in Section 3.1. The selected reference tile was changed from the last tile in the array, number 128, to the first tile in the array, number 1.

After switching the reference tile, 1 025 of the 2 657 GAMA9 observations were reprocessed in which 392 failed. For GAMA23, 322 of the 2 136 observations were reprocessed with 210 failing. Each successfully processed observation was then visually inspected in which 221 GAMA9 observations showed significant imaging artefacts and were excluded from consideration for the final mosaic. The distortion issues were not investigated further as thousands of observations were successfully processed and it was

[j] https://github.com/johnsmorgan/mwa_pb_lookup.

[k] https://github.com/nhurleywalker/fits_warp.

[l] https://gitlab.com/Sunmish/flux_warp.

https://doi.org/10.1017/pasa.2026.10245 Published online by Cambridge University Press

Table 3. The number of observations that were successfully processed. The first column is the description of the processing stage, the second column is the results for GAMA9 and the third column is the results for GAMA23.

Processing stage	GAMA9	GAMA23
Total number of observations	2 657	2 136
Successfully processed with first reference tile	1 632	1 814
Successfully processed with last reference tile	633	112
Failed processing	392	210
Failed visual inspection	221	0
Total successfully processed	2 044	1 926

unlikely that recalibrating this small group of observations would provide a significant improvement to the final mosaic. No problematic observations were observed for GAMA23. This resulted in a total of 2 044 valid observations for GAMA9 and 1 926 observations for GAMA23, as presented in Table 3.

4. Mosaicking

On completion of the processing of the observational data with `DIP`, the resulting images were co-added to produce the deep field images for each GAMA field. To produce a more consistent and predictable point spread function (PSF) and improve angular resolution, we select observations based on restoring beam dimensions. To keep the noise low, there is a trade-off between smaller beam size or a larger number of images. With this large number of observations, where confusion noise is important, co-addition of all images can have a negative effect, potentially increasing the final noise level. Therefore, it was necessary to attempt to find the balance by trying to select only observations that would improve the noise level in the final deep image while optimising the beam size to improve the resolution in the final mosaics.

4.1. Beam cuts

To optimise the beam size for the final mosaic of each region, the observations were selected based on the dimensions of the Gaussian fits to the synthesised beam referred to as the restoring beam. A smaller beam size enables an improvement in angular resolution and in RMS due to lower classical confusion. Hereafter, we refer to this filtering process based on restoring beam dimensions as 'beam cuts'. Based on the distribution of the full width at half maximum (FWHM) beam parameters shown in Figure 1, we decided to cut larger beams in the following way. For GAMA9, as the beam is fairly elongated with a narrow range of restoring beam position angles ($B_{\rm pa}$), we decided to cut on the restoring beam's major axis ($B_{\rm maj}$) only as described in Table 4. For GAMA23 with a rounder beam and a wider range of position angles, we decided to cut on maximum beam size, i.e. a diagonal in $B_{\rm maj}$ v $B_{\rm min}$ parameter space ($B_{\rm maj} = -B_{\rm min} + C$) outlined in Table 5, where $B_{\rm min}$ is the minor axis for the restoring beam. Finally, the mosaic for each beam cut was produced in the same fashion as the final images (as outlined in Section 4.2) and the RMS estimated by `BANE` is presented in Table 5.[m] The average RMS measured within each GAMA region was then used to evaluate the effectiveness of the beam cut.

For GAMA9, the optimal beam cut with the lowest RMS was determined to occur at $B_{\rm maj}$ of 56.7″. This resulted in a total of 1 282 observations being included in the mosaic, representing 62.7% of the available observations and equates to 42.7 h of integration time. For the GAMA23 region, the optimal beam cut resulting in the lowest RMS occurred for a linear cut of $B_{\rm maj} = -B_{\rm min} + 94.5$. This resulted in 1 701 observations (88.3% of the total available) selected for the mosaic, equating to an integration time of 56.7 h.

4.2. Co-addition

The observations were reprojected and regridded using `SWARP` (Bertin et al. 2002) with a `ZEA` projection. Within the same operation, the observations were co-added together utilising the RMS maps generated by `BANE` for each observation to calculate the pixel weighting and produce the deep field images. This co-addition step is near-equivalent to applying Equation (1) to all linear polarisations; however, utilising `SWARP` automates the resampling and re-projection.

[m] We originally attempted to convolve observations to a common beam; however, this introduced an offset into the flux density scale and therefore was not performed in the final deep field mosaics.

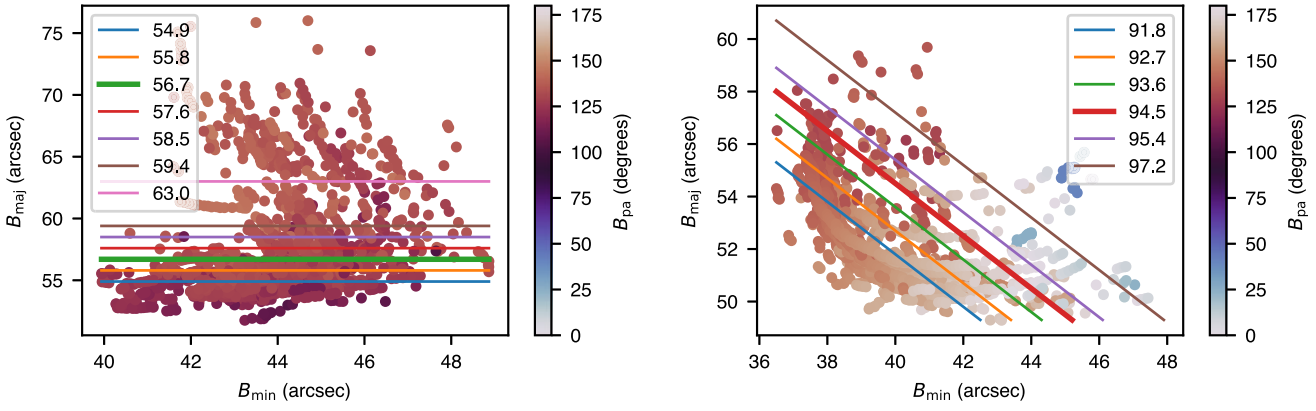


Figure 1. Beam cuts (solid lines) applied on the GAMA9 observations (left) and GAMA23 (right) where the *x*-axis represents the minor axis for the beam and the *y*-axis represent the major axis. For GAMA9, the cuts were applied on the $B_{\rm maj}$, where the cut at 56.7″ (green line) produced the optimum final RMS. For GAMA23, the beam cuts were based on the linear equation $B_{\rm maj} = -B_{\rm min} + C$ where the cut at $C = 94.5''$ (red line) produced the optimum final RMS.

https://doi.org/10.1017/pasa.2026.10245 Published online by Cambridge University Press

Table 4. GAMA9 beam cuts where the first column is the B_{maj} for the cut, the second is the number observations selected from the cut to the 2 044 available observations and the third is the average RMS measured within the GAMA9 region.

B_{maj} (arcsec)	# Obs selected	Mean RMS (mJy/beam)
54.9	591	0.797
55.8	1 040	0.769
56.7	1 282	0.755
57.6	1 450	0.760
58.5	1 536	0.760
59.4	1 642	0.762
63.0	1 820	0.778

Table 5. GAMA23 beam cuts where the first column is the value of the constant C in the linear equation $B_{maj} = -B_{min} + C$ used to filter the observations. The second column is the number of observations selected from the cut to the 1 926 available observations and the third column is the average RMS measured within the GAMA23 region.

C	# Obs selected	Mean RMS (mJy/beam)
91.8	865	0.349
92.7	1 295	0.335
93.6	1 610	0.333
94.5	1 701	0.331
95.4	1 792	0.334
97.2	1 867	0.360

The resulting GAMA23 mosaic from the MIDAS survey covered an area ∼850 deg^2 centred on GAMA23. Due to the larger area of the individual snapshots and a larger scatter in pointing centres, the GAMA9 mosaic covered a slightly larger area of ∼1 250 deg^2 centred on GAMA9. The image sizes for the mosaics were 9 316 pixels × 7 301 pixels for GAMA23 and 9 980 pixels × 9 980 pixels for GAMA9.

4.3. Calculating the point-spread-function

Due to the varying restoring beam shapes and sizes for the individual observations, the PSFs for the MIDAS mosaics while being very close to Gaussian, have an unpredictable shape. Therefore, we estimated the PSF using the same methods as described by Hurley-Walker et al. (2017), measuring the shapes and sizes of known unresolved sources to determine the effective PSF dimensions. To ensure the final PSFs could be approximated as Gaussian, we stacked 2D models of all restoring beams obtained by WSCLEAN for each observation within a MIDAS mosaic. We fit a 2D Gaussian to the resulting averages for GAMA9 and GAMA23. We subtracted the fitted 2D Gaussians from the MIDAS average beams and inspected the residuals which had a peak < 1% of the beam. This demonstrated that the final expected beam for each mosaic can be well described by a 2D Gaussian.

For each mosaic, we generated a source catalogue with `AEGEAN` and matched to the higher-resolution NVSS and SUMSS catalogue of unresolved sources described in Section 3.3, filtering for sources with an SNR > 10. We then created the PSF maps by calculating a HEALPix[n] map of the average measured source dimensions. The resulting PSF maps were used for source finding with `AEGEAN` on the MIDAS mosaics outlined in Section 5.2.

4.4. Ionospheric corrections

Small residual ionospheric effects in each observation can slightly vary source positions and introduce blurring into the mosaics. Although the changes in the shape of the PSF resulting from the blurring are measured in Section 4.3, it results in an underestimation of the measured peak flux density (while conserving total flux density). Following the methods used by Hurley-Walker et al. (2022), we correct this effect by normalising the flux density scales in the MIDAS mosaics. We created maps for the theoretical PSFs for each deep field image by mosaicking the PSF maps for the reprojected snapshots generated in Section 4.2. `AEGEAN` was run using the theoretical PSFs to measure source dimensions; the resulting catalogues were filtered to bright unresolved sources through the methods used in Section 4.3. A positional 'blurring' factor was calculated from the catalogues by

$$A = \frac{F_{maj} F_{min}}{T_{maj} T_{min}} \tag{2}$$

where F_{maj} and F_{min} represent the FWHM of the major and minor axes fitted to the sources, and T_{maj} and T_{min} represent the FWHM of the major and minor axes of the theoretical PSF. This resulted in positional blurring maps for each MIDAS mosaic shown in Appendix B, where the average blurring factor for GAMA9 was 1.10 and GAMA23 was 1.15. The MIDAS mosaics were then multiplied by their respective blurring map, bringing the integrated and peak flux densities into alignment.

5. Results

The processing resulted in a ∼1 250 deg^2 deep field mosaic centred around GAMA9 (RA +135°, Dec +0.5°) and a ∼850 deg^2 deep field mosaic centred around GAMA23 (RA +345°, Dec −32.5°). In Figure 2, we present a cutout of the resulting 60 deg^2 GAMA9 and GAMA23 regions from the MIDAS mosaics.

5.1. Noise analysis

5.1.1. Measured noise

To determine the effectiveness of the mosaicking process in reducing the RMS, we performed a jack-knifing test for each GAMA field. We generated mosaics with varying numbers of included observations in a range from four to the maximum available, doubling the number of observations included each time. For each increment of the number of observations included, we created 100 mosaics with the included snapshot images being selected randomly from the total available. All observation snapshots used in the mosaics were resampled to the same grid.

The noise for each mosaic was estimated with `BANE`, measuring the average RMS in each GAMA region. The results are shown in Figure 3, which shows the effect of a limiting noise on the mosaics. For both fields, the noise decreases as expected theoretically (i.e. as the square-root of the number of observations), but then deviates with the co-addition of more than 16 snapshots for GAMA23 and more than 64 for GAMA9. Hence, the thermal noise dominates down to these levels, but after mosaicking more than 64–128 snapshot images, the decrease in RMS reduction tapers off considerably

[n] Hierarchical Equal Area isoLatitude Pixelation (Gorski et al. 2005) available from http://healpix.sourceforge.net/.

https://doi.org/10.1017/pasa.2026.10245 Published online by Cambridge University Press

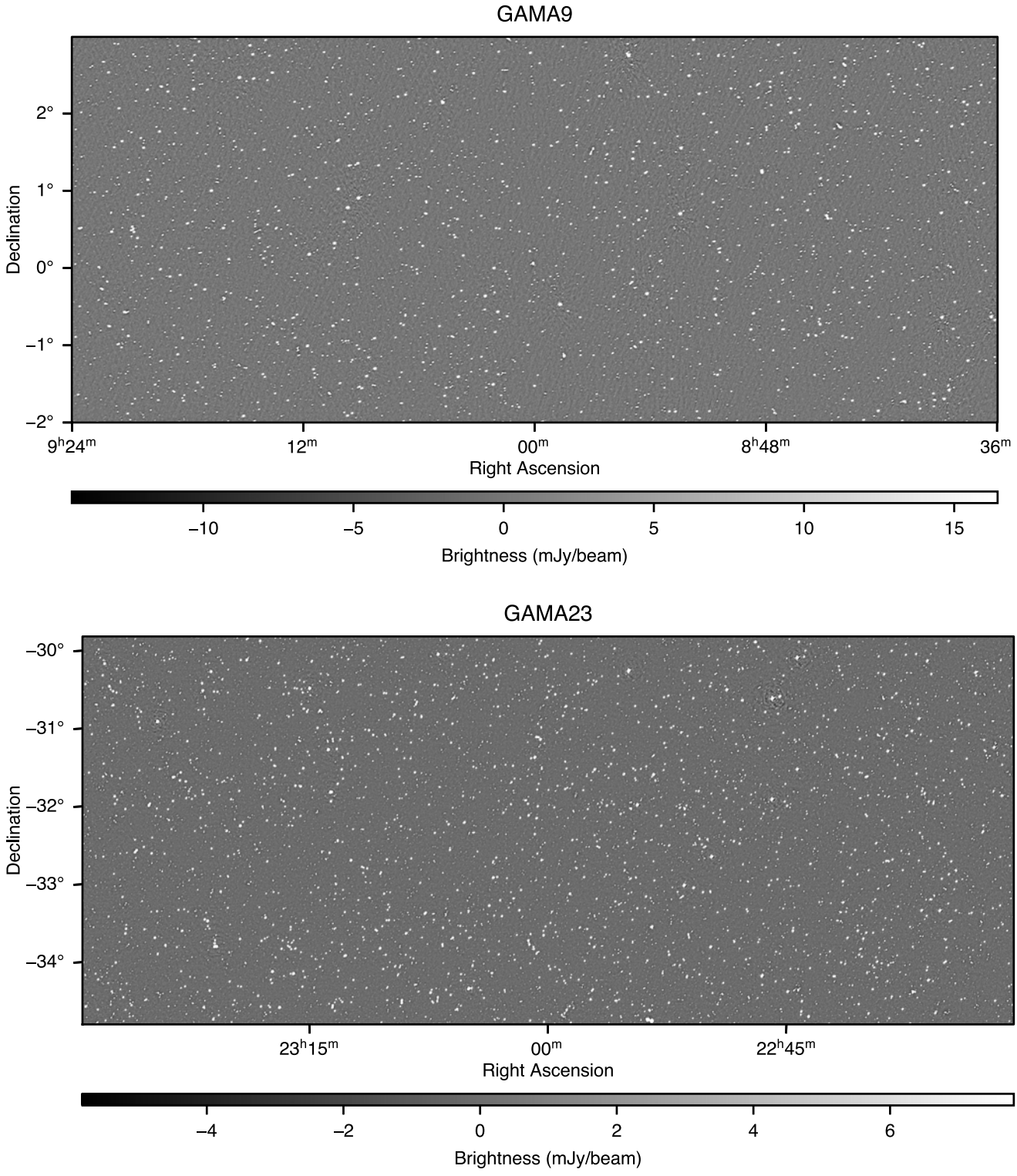


Figure 2. Greyscale cutouts of the 60 deg^2 GAMA9 region (top) and 60 deg^2 GAMA23 region (bottom) from the MIDAS mosaics.

suggesting that the fields are reaching a confusion limit, which is likely a combination of sidelobe and classical confusion. The lower decrease in RMS observed in the GAMA9 field was likely caused by a higher sidelobe confusion from the large number of bright sources in the field.

Estimation of the final noise in the GAMA23 deep field mosaic is difficult because the image approaches the classical confusion limit. `BANE` does not naturally function in this regime as it expects sparse input images dominated by Gaussian thermal noise. For this reason, we used `BANE` to characterise the structure of the noise

https://doi.org/10.1017/pasa.2026.10245 Published online by Cambridge University Press

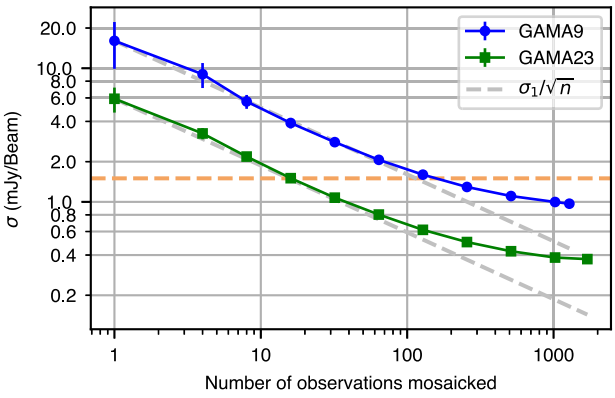


Figure 3. Jackknife plot for the mean RMS measured at the centre of the mosaic (*y*-axis) vs the number of observations mosaicked (*x*-axis). Each increment of the observation count was mosaicked 100 times with a randomised observation selection. The dashed grey lines represent the theoretical optimum noise reduction by the square-root of the number of observations. The dashed sandy brown line represents the median RMS achieved in GLEAM-X DRII (1.5 mJy/beam). The RMS reductions follows the theoretical optimum noise reduction for a mosaic count up to 64 snapshots for GAMA23 and 128 snapshots for GAMA9. After this point, as further snapshots are mosaicked, the RMS reduction tapers off indicating it has reached the sidelobe and/or classical confusion limit.

while implementing a novel approach to estimate the magnitude for the MIDAS mosaics.

We masked known sources in the 5° × 12° GAMA23 region of our deep image using a higher frequency, deeper image produced from the EMU survey by:

- Convolving the EMU deep field image of the GAMA23 region at 887.5 MHz produced by Gürkan et al. (2022) to the same beam size as the GAMA23 MIDAS mosaic.
- Re-projecting the convolved and the original EMU mosaics to the same pixel grid as the GAMA23 MIDAS mosaic.
- Masking pixels in the MIDAS GAMA23 mosaic where there was a corresponding pixel above the reported 5σ threshold (5×0.038 mJy/beam) in either the original EMU mosaic, or the convolved EMU mosaic. This is equivalent to 5×0.12 mJy/beam at the 215.68 MHz observed in MIDAS assuming a spectral index of $\alpha = -0.8$.
- Dilating all masked pixels with a fully connected 3×3 structure function for two iterations using the `scipy ndimage` Python package.

This resulted in 49% of the GAMA23 region being masked with the remaining unmasked pixels in the region consisting mainly of noise. An example cutout of the implemented filter is presented in Appendix A1 exhibiting its effectiveness in removing sources.

A histogram of the remaining pixels was plotted with a bin size of 5 μJy/beam and then a Gaussian fitted with `scipy curve_fit` as seen in Figure 4 with the resultant values described in Table 6. A Gaussian with a zero point $x_0 = -96 \pm 1$ μJy/beam and $\sigma = 331 \pm 1$ μJy/beam provided a very good fit with a small amount of additional positive flux observed due to incomplete masking. The masking of the bright areas leaves the underconvolved negative sidelobes of each bright source resulting in a 96 μJy/beam offset to the zero point. This offset value is arbitrary and does not offer any meaningful insight. Therefore, we concluded the RMS within the GAMA23 region is 0.331 ± 0.001 mJy/beam.

Table 6. The resultant values calculated in Section 5.1 for a Gaussian fitted to the remaining pixel's values in the GAMA9 and GAMA23 mosaics after filtering out sources, used to estimate the RMS of the mosaics. The first column is the region mosaicked, the second column is the estimated classical confusion noise, the third is the theoretically predicted RMS calculated by Equation (4), the fourth is the x_0 value of the fitted Gaussian and the fifth is the reported σ.

	Predicted (mJy/beam)		Measured (mJy/beam)	
Mosaic	σ_{conf}	σ_p	x_0	σ
GAMA9	0.358	0.833	-0.171 ± 0.001	0.923 ± 0.003
GAMA23	0.231	0.371	-0.096 ± 0.001	0.331 ± 0.001

To map the structure of the noise in the GAMA23 mosaic, `BANE` was run on the deep image with the default arguments. We then applied the same mask used to measure the RMS in the deep image to the RMS map output by `BANE`. The median value for the unmasked pixels in the GAMA23 region was then used to determine the scaling factor $f = \sigma/\tilde{i}$ where σ is the RMS determined from the Gaussian fit and $\tilde{i}$ is the median of the GAMA23 region in the masked RMS map. The entire RMS map was then multiplied by the scaling factor, calculated as $f = 0.81$, to determine the RMS distribution in the GAMA23 deep field image.

Due to the lower elevation of the GAMA9 field, the resulting RMS is higher with a larger combined natural and sidelobe confusion limit. In addition, the sidelobe noise is spatially correlated to the noise in the mosaic. The same methods that were used to calculate the RMS for the GAMA23 mosaic were used for the GAMA9 deep image.

A higher frequency deep ASKAP image mosaic for this field has not been published; however, the project 'Survey with ASKAP of GAMA-09+X-ray' (SWAG-X; Moss et al. 2020) has produced several tiles of this region. To create the base image required for the mask, we obtained seven tiles around GAMA9 from the SWAG-X survey that were conducted with ASKAP at 887.5 MHz. We then co-added the tiles with `SWARP` and estimated the RMS with `BANE`, using the mean of the RMS within the GAMA9 deep field ($\sigma = 0.054$ mJy/beam) to set our threshold of 5σ for the pixel masking. The resultant mask covered 65% of the GAMA9 deep field.

A Gaussian with $x_0 = -0.171 \pm 0.001$ mJy/beam and $\sigma = 0.923 \pm 0.001$ mJy/beam was fit to the histogram of the masked region. As was done with the GAMA23 deep image, `BANE` was run on the GAMA9 image and the RMS map was scaled accordingly with a calculated scale factor $f = 0.89$. The resulting RMS is significantly higher than the GAMA23 image due to the observing limitations of the field. The off-zenith observations result in a higher RMS, then the addition of the bright sources in the sidelobes increases the RMS even further while additionally introducing a noise structure to the mosaic. This constraint on the RMS is corroborated when examining the ratios between the GAMA fields for the average RMS of the individual snapshots (outlined in Table 1) and the ratio of the RMS for the final mosaics (outlined in Table 6), where $\sigma_{G9}/\sigma_{G23} = 2.8$ for both.

Due to the attenuation of the primary beam, the RMS increases significantly at the edges of each mosaic as seen in Figure 5. In the GAMA23 deep field image, the RMS reaches close to 6 mJy/beam at the edge while in the GAMA9 mosaic the RMS increases to slightly over 10 mJy/beam at the edge. However, due to the large

https://doi.org/10.1017/pasa.2026.10245 Published online by Cambridge University Press

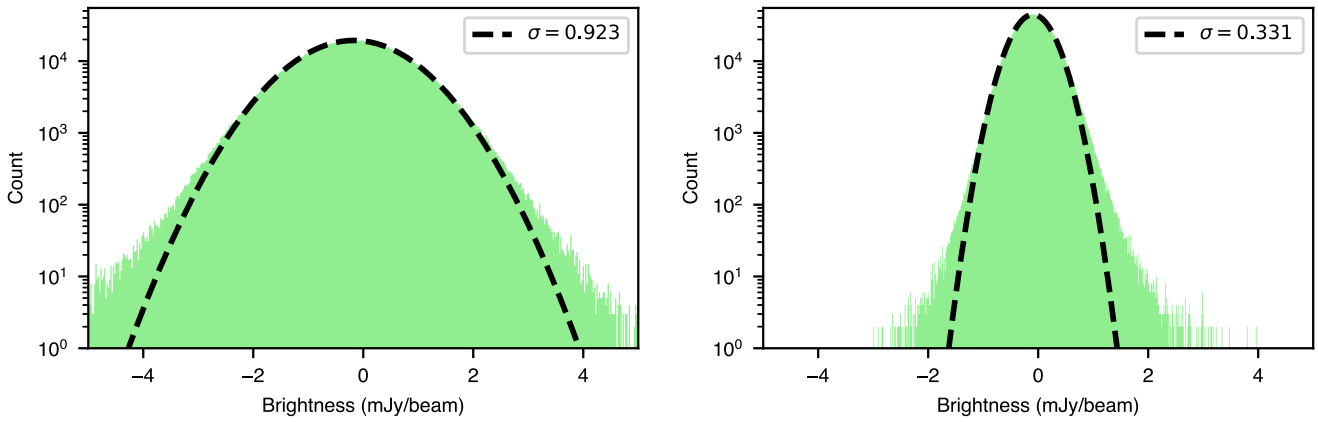


Figure 4. Distribution of the pixel intensity in the GAMA9 region (left) and GAMA23 region (right) as a function of flux density for the deep images after masking all pixels above 5σ in the EMU image. In the GAMA9 histogram, the black dashed line is a Gaussian with $x_0 = -0.171$ mJy/beam and $\sigma = 0.923$ mJy/beam fit to the histogram. For the GAMA23 image, the black dashed line represents a Gaussian with $x_0 = -0.096$ mJy/beam and $\sigma = 0.331$ mJy/beam.

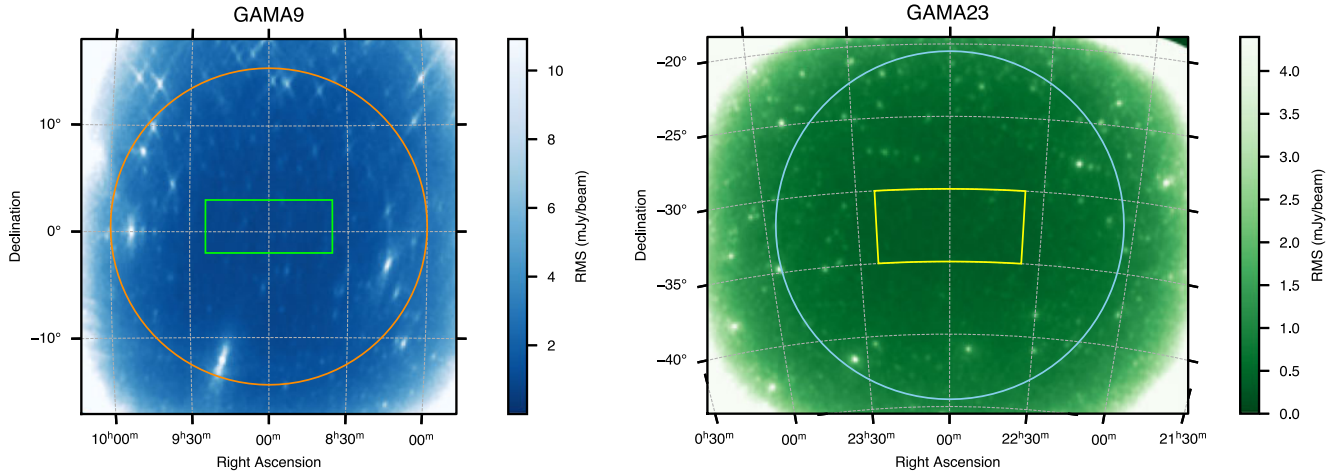


Figure 5. RMS maps for the GAMA9 (left) and GAMA23 (right) MIDAS mosaics where the rectangles represent the regions targeted with GAMA9 in green and GAMA23 in yellow. The circles represent the area used for the completeness estimation and source counts for GAMA9 (orange) and GAMA23 (blue).

field-of-view of the MWA, the RMS in the central 60 deg^2 GAMA fields remain relatively uniform.

5.1.2. Theoretical noise

We estimated the theoretical classical confusion noise ($\sigma_{\rm conf}$) for each MIDAS mosaic using the methods derived by Condon (1974) where

$$\sigma_{\rm conf} = \left(\frac{q^{3-\gamma}}{3-\gamma}\right)^{\frac{1}{\gamma-1}} \left(k\frac{\pi\ B_{\rm maj}B_{\rm min}}{4(\gamma-1)\ln(2)}\right)^{\frac{1}{\gamma-1}} \quad (3)$$

in which $B_{\rm maj}$ and $B_{\rm min}$ are the major and minor axes for the average restoring beam obtained by WSCLEAN from the final fitted PSF listed in Table 8 and q is the SNR that we take to be $q = 1$ at the confusion limit. Using the LOFAR power-law source counts by Williams et al. (2016), we estimate the normalisation $k = 4 \times 10^{-6}$ with the source count slope $\gamma = 1.5$ at flux densities around 1 mJy. Note this slope has a conservatively steep value as the two fields only just reach the up-turn in the source counts at this flux density.

Combining the theoretical classical confusion noise with the theoretically optimal noise for n number of observations mosaicked using the mean RMS from the individual snapshots ($\overline{\sigma_1}$) where

$$\sigma_p = \frac{(\overline{\sigma_1} - \sigma_{\rm conf})}{\sqrt{n}} + \sigma_{\rm conf} \quad (4)$$

resulted in the predicted RMS (σ_p) for the MIDAS mosaics listed in Table 6. However, this estimation does not account for sidelobe confusion that dominates GAMA9. Additionally, the confusion noise is highly sensitive to the source count slope which is rapidly changing at the faintest fluxes. We observe agreement with our predictions for GAMA23, while GAMA9 is slightly underpredicted as expected due to the large amount of sidelobe noise contributed by Hydra-A.

After scaling by a common spectral index ($\alpha = -0.8$ for $S_\nu \propto \nu^\alpha$) and comparing to wide-field (>60 deg^2) radio surveys in the Southern hemisphere, Figure 6 shows that the GAMA9 mosaic reaches a depth deeper than GLEAM (Hurley-Walker et al. 2017, 2019), GLEAM-X (Hurley-Walker et al. 2022; Ross et al. 2024) and GLEAM-300 (Duchesne et al. 2025a). It achieves an RMS comparable to surveys such as the Rapid ASKAP Continuum Survey (RACS-low; McConnell et al. 2020, RACS-mid; Duchesne

https://doi.org/10.1017/pasa.2026.10245 Published online by Cambridge University Press

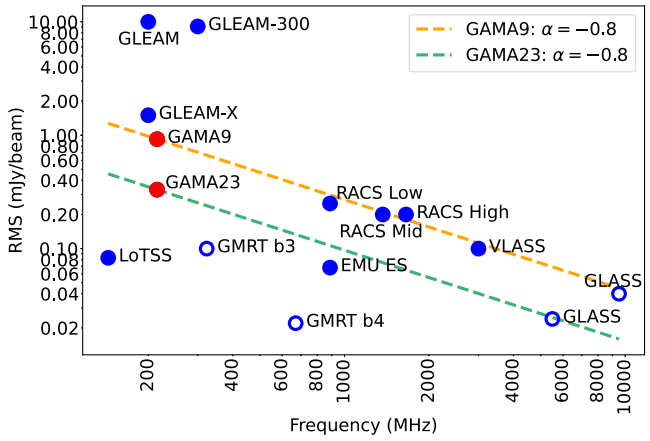


Figure 6. Comparison of the 215.68 MHz MIDAS GAMA9 and GAMA23 deep images to wide-field surveys (>60 deg^2) performed at radio wavelengths assuming a constant spectral index of $\alpha = -0.8$. Here the *x*-axis represents the wavelength of the survey measured in MHz and the *y*-axis reflects the RMS of the deep field image measure in mJy/beam. The solid circles are completed published surveys while the open circles are estimations for unpublished surveys currently in progress.

Table 7. The number of sources detected within each survey, and the rows represent each cut that was applied. Each column lists the numbers of sources remaining after each cut where the full image columns are the number of sources within the full survey mosaic and the region columns are the number of sources within the GAMA9 (RA +129° to +141°, Dec −2° to +3°) and GAMA23 (RA +339° to +351°, Dec −35° to −30°) regions, respectively.

	GAMA9		GAMA23	
Cut	Full image	Region	Full image	Region
Initial	67 985	5 043	106 221	10 591
$S_{peak} < 5\sigma$	53 515	4 227	80 523	8 423
On edge	53 431	4 227	80 428	8 423
$S_{int}/S_{peak} > 16$	53 419	4 225	80 407	8 417

Table 8. The beam dimensions calculated from the source dimensions of unresolved sources in the MIDAS catalogues along with the resultant beams per source calculated for each GAMA field's mosaic.

Field	B_{maj} (arcsec)	B_{min} (arcsec)	B_{pa} (degrees)	Beam area (deg^2)	Beams per source
GAMA9	64.3	48.7	−66.1	2.73×10^{-4}	52.0
GAMA23	57.3	43.9	−27.4	2.20×10^{-4}	32.4

et al. 2023, RACS-high; Duchesne et al. 2025b) and the Very Large Array Sky Survey (VLASS; Lacy et al. 2020), probing a lower-frequency complementary range. However, the GAMA23 mosaic probes significantly deeper, offering a depth comparable to the expectant GAMA Legacy ATCA Sky Survey (GLASS; Huynh et al. in prep) and close to the 887.5 MHz early EMU release (Norris et al. 2021). However, the MIDAS mosaics are much shallower than the LoTSS survey (Shimwell et al. 2017, 2019, 2022) of the northern sky and the expected RMS for the Giant Metrewave Radio Telescope (GMRT; Seymour et al. 2020) survey.

The MIDAS 215.68 MHz deep field data along with the plethora of higher frequency data available for the GAMA23 field offers an opportunity to probe this area of the sky further with the potential for new insight into galaxy clusters, halos, relics, AGN and more.

5.2. Source catalogues

The source catalogues for the MIDAS GAMA9 and GAMA23 surveys were created with `AEGEAN` using a blind source finding method. We used `AEGEAN`'s default parameters except for the `seedclip`, PSF, RMS, and background values. The `seedclip` was set to 4σ to detect pixels above this flux density for initial positions used in the component fitting. For the additional parameters, we utilised the PSF generated in Section 4.4 along with the rescaled RMS map and the constant background value calculated in Section 5.1. This resulted in a total of 67 985 sources found in the GAMA9 mosaic and 106 221 sources found in the GAMA23 mosaic, where we define a source as an individual fitted Gaussian component. The catalogues were reduced to sources with a peak flux density above the 5σ detection level where the RMS is determined from the rescaled RMS maps produced in Section 5.1. Next, the sources within 1′ from the edge of the mosaic were removed from the GAMA catalogues to ensure that there were no sources with flux density overlapping the edge of the mosaic.

We visually inspected sources with high integrated to peak flux density ratios in both MIDAS mosaics. It was determined all sources with a ratio $S_{int}/S_{peak} > 16$ were spurious and therefore removed from the catalogues. Due to the higher noise around bright sources caused by sidelobes, sources nearby are difficult to validate as they could be artefacts from the sidelobes. As a precaution, we flagged sources that were within 4′ of a 1.5 Jy sources as lower reliability. As a result, 429 sources in the GAMA9 catalogue and 852 sources in the GAMA23 catalogue were flagged.

As detailed in Table 7, this resulted in a total of 53 419 sources in the final GAMA9 catalogue and 80 407 sources in the GAMA23 catalogue. The 24 column names in the MIDAS catalogues are outlined in Appendix C. For GAMA9, 3.4% of islands were multi-component while 5.0% of the islands in GAMA23 had multiple components.

The average beam dimensions were calculated from the source dimensions of compact sources within the MIDAS catalogues selected with the RMS envelope described in Section 5.3. The average B_{maj} and B_{min} for sources within the respective GAMA regions were calculated and are outlined in Table 8. Within the GAMA9 region, 4 225 sources were detected with a beam size of 2.73×10^{-4} deg^2 for the mosaic, resulting in a source density of 70.42 sources/deg^2 (52.0 beams per source[o]). However, a much larger number of sources were detected within the GAMA23 region with a total of 8 417 sources. With a beam size of 2.20×10^{-4} deg^2 for the mosaic, we approach the classical confusion limit with a source density of 140.28 sources/deg^2 (32.4 beams per source).

5.3. Flux density scale evaluation

To evaluate the flux density scales of our catalogues, we compared the MIDAS catalogues to the wideband integrated flux densities from the GLEAM catalogue (Hurley-Walker et al. 2017) and to the GLEAM-X DRII catalogue (Ross et al. 2024) for GAMA23. The GLEAM(-X) flux densities were scaled to 215.68 MHz using an

[o]This is a classical measure of how dense the field is, where 30 and less is a typical value for classical confusion.

https://doi.org/10.1017/pasa.2026.10245 Published online by Cambridge University Press

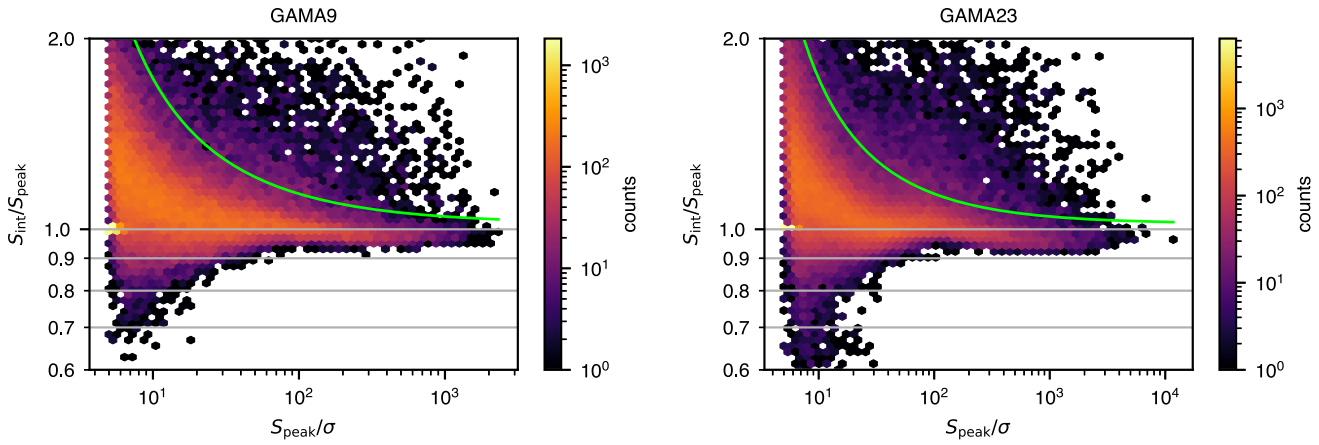


Figure 7. Ratio of integrated flux density to peak flux density as a function of SNR for the MIDAS GAMA9 (left) and GAMA23 (right) source catalogues. The green line is the upper envelope, Equation (5), set to define the limit for unresolved sources that we approximate to be 95% of the total sources. The small bump observed in GAMA23 around $S_{peak}/\sigma \approx 100$ and the less noticeable bump observed in GAMA9 around $S_{peak}/\sigma \approx 60$ is suspected to be a result of sources on the detection limit in the individual observations; these sources would be deconvolved in some observations, but not in others.

assumed constant spectral index of $\alpha = -0.8$. At the time of writing, there are no public data releases from GLEAM-X that cover the GAMA9 field.

The MIDAS catalogues were matched to GLEAM(-X) with a maximum separation distance of 1′. The MIDAS catalogue was reduced to only include compact source, additionally any MIDAS source with a neighbour within 2′ was removed to ensure that sources within the GLEAM(-X) catalogues were not resolved into multiple sources within the MIDAS catalogues. Compact sources were selected from the catalogue based on their integrated flux density to peak flux density ratio. We plotted the ratios as a function of SNR as seen in Figure 7 where we estimated an upper envelope of

$$\frac{S_{\rm peak}}{S_{\rm int}} = 0.98 - \frac{1.6}{(S_{\rm peak}/\sigma)^{0.6}} \tag{5}$$

to capture 95% of the sources, where $S_{\rm peak}$ is the measured peak flux, $S_{\rm int}$ is the measured integrated flux and σ is the measured local RMS. A small bump is observed in the ratios around $S_{\rm peak}/\sigma \approx 60$–$100$ that is likely caused by unCLEANed sources. The masking stage discussed in Section 3.2.2 results in only sources $> 3\sigma_i$ being CLEANed (where σ_i is the local RMS in an individual 2-min snapshot). Therefore, sources with a flux density near this detection limit will be CLEANed in some snapshots and not others, resulting in more unpredictable source morphologies after mosaicking. Sources below this detection limit will not be CLEANed at all.

A correctable bias in the flux density measurements can be introduced from measurement errors known as Eddington bias (Eddington 1913). Flux density measurements for sources will scatter above and below their true values. As there are a greater number of the fainter sources (due to the steep source counts) that will be measured brighter than there are bright sources that will be measured fainter, the flux density measurements for the faint sources are much more likely to be overestimated. To evaluate the Eddington bias in our flux density scale comparisons, we use the maximum-likelihood value ($S_{\rm ml}$; Hogg & Turner 1998; Hurley-Walker et al. 2017),

$$S_{\rm ml} = \frac{S}{2} + \frac{S}{2}\sqrt{1 - \frac{4q+4}{(S/\sigma)^2}} \tag{6}$$

where S is the measured integrated flux density, σ is the local RMS measured for the source, and $q = 1.54$ is the logarithmic source count slope at the GLEAM flux densities (Franzen et al. 2016; Hurley-Walker et al. 2022; Ross et al. 2024). This correction made a negligible difference in our results so we chose not to apply it.

The flux density scale comparisons with GLEAM(-X) in Figure 8 exhibits good agreement with GLEAM. For GLEAM-X DRII, we observe agreeance at an SNR $> \sim$100; however, at lower SNR values, we observe a discrepancy where GLEAM-X reports lower source flux densities. This is likely due to the CLEANing methods used in GLEAM-X where a 3σ `auto-mask` was used. As discussed in Section 3.2.2, we found this level of `auto-mask` would CLEAN noise peaks removing flux from real sources and introduce a small offset into the flux density measurements. This results in an under-prediction of flux density, which is more evident for fainter sources and aligns with the observed discrepancy.

The flux density scaling for MIDAS was performed using GLEAM as a reference during post-imaging as described in Section 3.3. GLEAM reports an uncertainty of 8% for its flux density scale accuracy, therefore we prescribe an 8% uncertainty for the MIDAS flux density scaling when compared to other surveys.

5.4. Astrometry

The precision of the astrometry for the final MIDAS GAMA9 and GAMA23 source catalogues was evaluated by comparing the source positions with the joint NVSS and SUMSS positional-based catalogue of unresolved sources described in Section 3.3, which we will refer to as the reference catalogue. The GAMA deep field catalogues were reduced to sources $> 50\sigma$ and matched to the reference catalogue with a matching distance within 1′, where the source positions in the reference catalogue were assumed to be the correct positions. We then calculated the offsets for the deep field sources relative to the reference sources and calculate the mean offset and standard deviation for the offset per catalogue.

For the GAMA9 catalogue, there were a total of 8 749 sources above 50σ matched to the reference catalogue. The resulting mean RA offset was $+0.007'' \pm 0.706''$ and the mean Dec offset was $+0.002'' \pm 1.440''$ as seen in Figure 9.

The GAMA23 catalogue matched 13 355 sources above 50σ to the reference catalogue. As seen in Figure 9, an average RA

https://doi.org/10.1017/pasa.2026.10245 Published online by Cambridge University Press

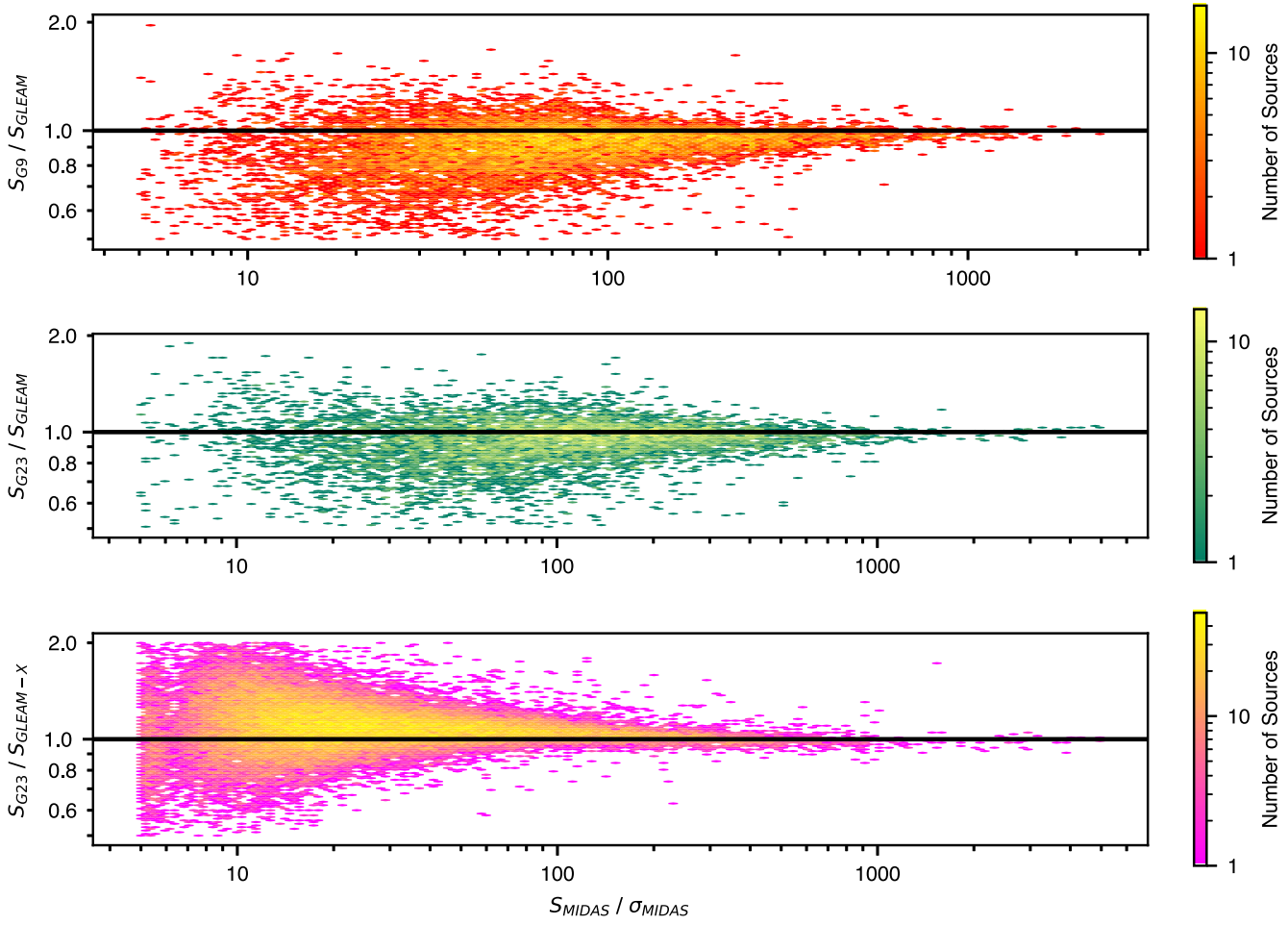


Figure 8. The integrated flux density ratios between GLEAM and GAMA9 MIDAS at the top, GLEAM and GAMA23 MIDAS in the middle and GLEAM-X and GAMA23 MIDAS at the bottom. The *x*-axes represents the MIDAS SNR and the *y*-axes is the flux density ratio between the surveys. The solid black line represent a ratio of 1. Here we observe good agreement with GLEAM through the entire flux density range. We observe agreement with GLEAM-X at an SNR $> \sim$100, however at lower SNR values GLEAM-X reports lower flux density scales. We attribute this to the `CLEAN`ing methods used in GLEAM-X resulting in an over-estimate of the observed vs true flux density values.

offset of $-0.009'' \pm 1.054''$ and a Dec offset of $+0.010'' \pm 1.149''$ was calculated.

We additionally confirm astrometry matching to RACS-high which offers a higher angular resolution of $11.8'' \times 8.1''$ but experiences astrometry limitations with positional uncertainties of $0.6''$ in right-ascension and $0.7''$ in declination (Duchesne et al. 2025b). An average RA offset of $+0.040'' \pm 3.916''$ and Dec offset of $-0.095'' \pm 3.666''$ was calculated between the GAMA9 catalogue and the RACS-high catalogue. For the GAMA23 catalogue, an average RA offset of $+0.24'' \pm 3.97''$ and a Dec offset of $-0.091'' \pm 3.904''$ was calculated. Due to the limitations of RACS-high, the results have large uncertainties; however, they are in good agreement.

5.5. Completeness

To estimate the percentage of true sources recovered at a given flux density, which we define as the completeness, we injected simulated sources into random positions in each deep field image at selected flux density levels. To accomplish this, we used `AeRes` from the `AEGEAN` package that enables adding or removing sources from an image with specified positions, flux densities, and shapes. We ran 26 simulations for flux density levels ranging from 1 to 316 mJy, evenly spaced in log space, injecting $\sim$10 point-like sources per square-degree at a constant flux density for each simulation.[P] To ensure that we were not introducing an unnecessary confusion measurement, a minimum separation distance between simulated sources was set at $5'$. No minimum separation distance was established between the simulated and real sources to ensure that the classical confusion limit was accurately taken into account.

Blind source finding with `AEGEAN` was run on each simulation and the percentage of injected sources recovered was calculated. To estimate the uncertainty for the completeness calculations, we ran the full simulation process 100 times for each region. The mean for each flux density level was then used for our completeness values and the standard deviation for the uncertainty.

The completeness curves for the GAMA regions are shown in Figure 10, although part of the shape of the curves will be due to

[P]Formally, the number of sources injected per flux density bin should vary per the source counts to obtain the most precise uncertainties. This was verified with a small number of simulations which confirmed that injecting more sources resulted in a consistent completeness, but reduced the uncertainties. However, this is compute intensive and testing demonstrated that the completeness uncertainties were always far less than the Poisson uncertainties so the extra precision was unnecessary.

https://doi.org/10.1017/pasa.2026.10245 Published online by Cambridge University Press

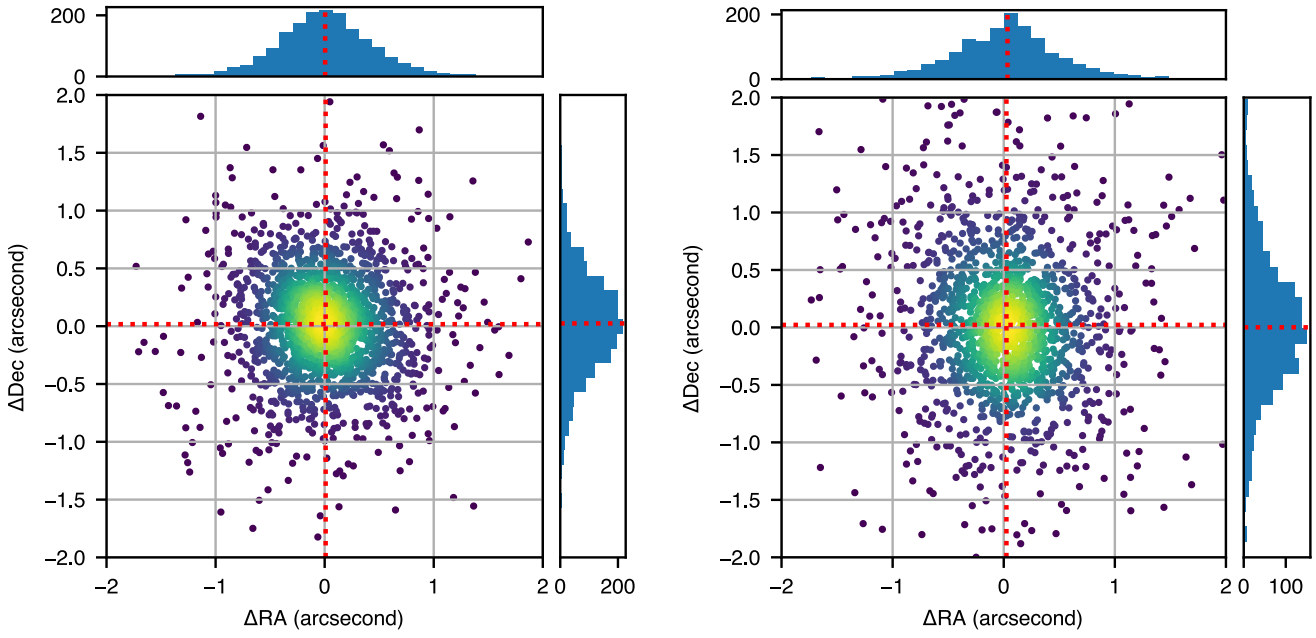


Figure 9. The astrometric offsets for the GAMA9 source catalogue (left) and GAMA23 source catalogue (right) compared to a reference catalogue containing unresolved sources from NVSS and SUMSS. The *x*-axes and *y*-axes are the offsets for the RA and Dec respectively measured in arcseconds. A total off 8 749 sources was compared resulting in an RA offset of $+0.007'' \pm 0.706''$ and a Dec offset of $+0.002'' \pm 1.440''$ for GAMA9 and a total 13 355 sources for GAMA23 resulting in an average RA offset of $-0.009'' \pm 1.054''$ and a Dec offset of $+0.010'' \pm 1.149''$. The red dotted lines represents the mean RA and Dec offsets.

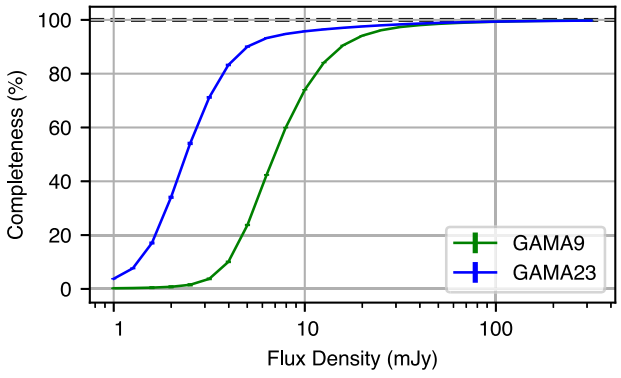


Figure 10. The completeness for a circular area with a radius of 15° in the GAMA9 (green) mosaic and a circle with a radius of 12° in the GAMA23 (blue) mosaic as a function of flux density. The errors were calculated as the standard deviation from 100 simulations. The dashed black line represents 100% completeness. A 90% completeness was estimated at ∼10.06 mJy for GAMA9 and ∼4.97 mJy for GAMA23.

the increase in the RMS towards the edges of the fields of view that is observed in Figure 5. To attempt to minimise this effect, we measure the completeness for a circular area in the centre of each region. For the GAMA9 field, a circular area with a radius of 15° was used resulting in an estimated completeness of 50% at ∼7.0 mJy and 90% at ∼15.6 mJy. A 12° radius was used for the circle at the centre of the GAMA23 region resulting in a completeness of 50% at ∼2.4 mJy and 90% at ∼5.0 mJy.

5.6. Source counts

The source counts for each deep field catalogue were calculated for a circular area at the centre of each GAMA region. For the GAMA9 mosaic, we used a circle with a radius of 15° centred at RA +135°, Dec +0.5°; for the GAMA23 mosaic, we used a circle with a radius of 12° centred at RA +345°, Dec −32.5° (i.e. the same regions over which we determined the completeness). The source Hydra-A was excluded from the GAMA9 MIDAS source counts as it is a very bright outlier. The sources detected in each circular region were binned by flux density level in 15 bins; the faintest 12 bins are equal size in log space, while the three brightest bins were double the size to account for the lower number of sources. The value for the start of the first bin was calculated as five times the average RMS of all selected sources, while the end of the final bin was set as the value of the brightest source.

The GAMA9 source catalogue was binned from 7.44×10^{-3} to 23.3 Jy with a bin width of $\Delta \log_{10}(S) = 0.194$ Jy for the first 12 bins and a width of $\Delta \log_{10}(S) = 0.388$ Jy for the brightest 3 bins. For GAMA23, we used a bin width of $\Delta \log_{10}(S) = 0.217$ in log-space for the first 24 bins and $\Delta \log_{10}(S) = 0.434$ Jy for the 3 brightest bins, covering a flux density range from 2.58×10^{-3} Jy to 21.0 Jy.

Here in Figure 11, we present the source counts for our deep field catalogues normalised to Euclidean values. These source counts have been corrected for the incompleteness calculated in Section 5.5 and are listed in Tables 9 and 10. The corrected normalised source counts (C_N) were calculated by

$$C_N = S^{2.5} \frac{dN}{a\, dS} \tag{7}$$

where S is the centre of the flux density bins in Jy, dN is the number of sources in the bin (N_s) multiplied by the correction factor for completeness calculated from the linear fit between the two closest flux density bins determined in Section 5.5, a is the area sampled in steradian, and dS is the width of the bin in Jy.

The uncertainty for the source counts was estimated using Poisson statistics for a confidence interval equivalent to a 1σ

https://doi.org/10.1017/pasa.2026.10245 Published online by Cambridge University Press

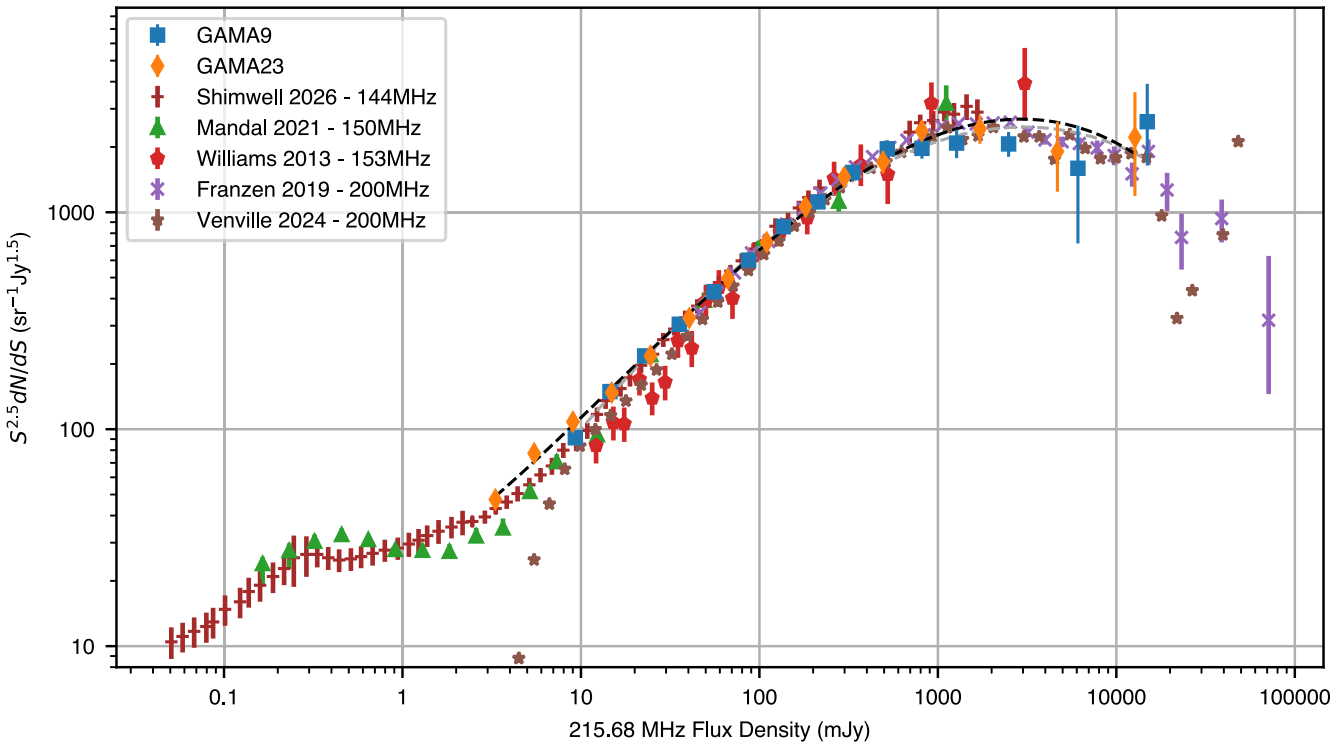


Figure 11. Source counts normalised to Euclidean values for GAMA9 (blue) and GAMA23 (gold) as a function of flux density in comparison to low-frequency counts from literature scaled to 215.68 MHz. Here we observe good agreement with the 200 MHz counts by Franzen et al. (2019), but a minor deviation from Venville et al. (2024) at a flux density below ∼40 mJy. We attribute this deviation to the lack of a completeness correction applied to their source counts. We observe good agreement with the 144 MHz source counts by Shimwell et al. (2026) with a slight deviation at the bright end with GAMA9 and a small deviation at the faint end with GAMA23 as it approaches the GAMA9 observing limit. Comparing to the ∼150 MHz counts by Mandal et al. (2021) and Williams et al. (2013), we observe agreeance down to ∼25 mJy. Below this we observe a deviation in the counts that is likely due to the differing resolutions and flux density limits of the surveys along with the different source finding methods employed. The black and grey dashed lines represent a fitted third-degree polynomial to the GAMA23 and GAMA9 source counts respectively.

Gaussian described by Gehrels (1986) where for the upper (λ_u) and lower (λ_l) limits,

$$\lambda_u \approx \sqrt{dN+1}+1$$
$$\lambda_l \approx \sqrt{dN-0.25}. \quad (8)$$

For large values of dN these uncertainties tend towards $\lambda = \sqrt{dN}$; however, these uncertainties are formally correct for $dN \lesssim 20$.

Additionally, we add cosmic variance to the uncertainty, which we calculate for each bin using the LOFAR Two-metre Sky Survey (LoTSS) Data Release 2 catalogue (Shimwell et al. 2022). The data release specifies a potential flux density variation dependant on pointing which may limit this analysis, but we continue with the assumption the effects are small. The flux density of these sources was scaled from 144 to 215.68 MHz under the assumption of a constant spectral index of $\alpha = -0.8$. The source counts for each bin in each region were measured for 100 randomly positioned circular areas within the area surveyed by LoTSS DR2. The size of the circles was equal to those that were used to measure the deep field GAMA source counts, 15° for GAMA9 and 12° for GAMA23. The centre location of the circles were determined by selecting random sources in the LoTSS catalogue. To ensure that the region was not on the edge of the measured field and had complete coverage, we searched an area of 2′ at the upper and lower extremes for the RA and Dec coordinates of the circle's edges to ensure there were sources present. The cosmic variance for the flux density bins below 2 Jy was calculated to be ∼5–10%, but for the brighter bins the cosmic variance increases significantly to ∼20–35%. The error on the corrected source counts was taken as the sum in quadrature of the Poisson error, completeness correction error, and uncertainty due to cosmic variance.

The resulting normalised source counts seen in Figure 11 are compared to the counts generated from other low-frequency surveys scaled by $\alpha = -0.8$. We can not compare source counts from surveys at very different frequencies due to selection biases resulting in changes to spectral index distribution between the frequency ranges. This means a simple spectral index conversion could not be used for comparison with surveys completed at frequencies significantly different from the 215.68 MHz we observed at (Kellermann 1964; Franzen et al. 2016). Unfortunately, no source counts have been previously calculated at 216 MHz, so we made comparisons with surveys conducted at 144, 150, 153, and 200 MHz.

For our comparisons, we used counts by Williams et al. (2013) who utilised observations of the National Optical Astronomy Observatory (NOAO) Boötes field with the Giant Metrewave Radio Telescope (GMRT) at 153 MHz producing an image reaching an RMS of 2 mJy/beam covering an area of 30 deg^2. Additionally, we included source counts at 200 MHz from Franzen et al. (2019) using the GLEAM survey that reaches an RMS of 10 mJy/beam and covers an area of 25 000 deg^2, which reduces potential influence of cosmic variance and improves accuracy at the bright end. We also include the 200 MHz source counts produced

https://doi.org/10.1017/pasa.2026.10245 Published online by Cambridge University Press

Table 9. The source counts calculated with the GAMA9 mosaic. The first column is the bin ranges, the second is the bin centres, and the third is the number of sources detected in the bin. The fourth column is the correction factor applied to the number of sources, calculated from the completeness presented in Section 5.5. The fifth column is the source counts normalised to Euclidean values along with their uncertainty estimated from Poisson statistics, the uncertainty due to cosmic variance and completeness errors added in quadrature.

Bin range S (mJy)	Bin centre S (mJy)	N_s	Correction factor	$S_c^{2.5}dN/dS$ ($\mathrm{sr}^{-1}\,\mathrm{Jy}^{1.5}$)
7.44–11.6	9.30	6 809	1.444 ± 0.004	$91.4^{+5.7}_{-5.7}$
11.6–18.2	14.54	7 218	1.137 ± 0.003	$149^{+8.5}_{-8.5}$
18.2–28.4	22.75	5 835	1.050 ± 0.002	218^{+12}_{-12}
28.4–44.5	35.58	4 281	1.024 ± 0.002	305^{+17}_{-17}
44.5–69.6	55.64	3 121	1.013 ± 0.001	430^{+25}_{-25}
69.6–109	87.02	2 244	1.008 ± 0.001	601^{+39}_{-39}
109–170	136.1	1 642	1.005 ± 0.001	858^{+67}_{-66}
170–266	212.8	1 095	1.003 ± 0.001	$1\,117^{+86}_{-86}$
266–416	332.9	767	–	$1\,526^{+132}_{-131}$
416–651	520.6	504	–	$1\,961^{+188}_{-187}$
651–1 018	814.2	259	–	$1\,971^{+209}_{-204}$
1 018–1 592	1 273	140	–	$2\,084^{+317}_{-307}$
1 592–3 895	2 490	104	–	$2\,065^{+281}_{-264}$
3 895–9 527	6 092	21	–	$1\,595^{+914}_{-877}$
9 527–23 303	14 900	9	–	$2\,615^{+1\,293}_{-973}$

Table 10. The source counts calculated with the GAMA23 mosaic. As with Table 9, The first column is the bin ranges, the second is the bin centres, and the third is the number of sources detected in the bin. The fourth column is the correction factor applied to the number of sources, calculated from the completeness calculated in Section 5.5. The fifth column is the source count normalised to Euclidean values along with their uncertainty estimated from Poisson statistics, the uncertainty due to cosmic variance and completeness errors added in quadrature.

Bin range S (mJy)	Bin centre S (mJy)	N_s	Correction factor	$S_c^{2.5}dN/dS$ ($\mathrm{sr}^{-1}\,\mathrm{Jy}^{1.5}$)
2.58–4.26	3.32	12 654	1.361 ± 0.005	$47.4^{+2.9}_{-2.9}$
4.26–7.02	5.47	12 115	1.097 ± 0.004	$77.4^{+3.9}_{-3.9}$
7.02–11.6	9.02	8 354	1.050 ± 0.003	$108^{+6.2}_{-6.2}$
11.6–19.1	14.87	5 468	1.032 ± 0.003	$147^{+9.5}_{-9.5}$
19.1–31.5	24.51	3 856	1.021 ± 0.002	218^{+14}_{-14}
31.5–51.9	40.42	2 740	1.014 ± 0.002	325^{+22}_{-21}
51.9–85.6	66.64	1 978	1.009 ± 0.001	495^{+36}_{-36}
85.6–141	109.9	1 378	1.006 ± 0.001	728^{+54}_{-53}
141–233	181.2	949	1.004 ± 0.001	$1\,059^{+86}_{-85}$
233–384	298.8	616	1.003 ± 0.001	$1\,454^{+135}_{-134}$
384–633	492.6	343	–	$1\,709^{+202}_{-200}$
633–1 043	812.2	225	–	$2\,374^{+255}_{-248}$
1 043–2 835	1 720	154	–	$2\,426^{+368}_{-359}$
2 835–7 708	4 675	27	–	$1\,907^{+710}_{-663}$
7 708–20 956	12 710	7	–	$2\,216^{+1\,359}_{-1\,026}$

by Venville et al. (2024) that utilises the central 5 600 deg^2 area of the GLEAM-X DR2 survey which contains the lowest and least variable RMS properties but do not correct for completeness. Finally, we included source counts produced from the LoTSS survey which offer better insight at the faint end. We include the 150 MHz counts by Mandal et al. (2021) that utilises the deep field observations from the survey reaching an RMS of 0.1 mJy/beam for a 25 deg^2 area along with the counts published in LoTSS-DR3 by Shimwell et al. (2026) covering 88% of the northern sky, achieving an average RMS of 0.092 mJy/beam.

Comparing to the 200 MHz counts, we see good agreement with Franzen et al. (2016) for the entire flux density range, reaffirming the alignment with GLEAM as observed in Section 5.3. The comparison with Venville et al. (2024) shows good agreement down to ∼40 mJy, below this level their source count slope becomes steeper. This is consistent with the lack of a completeness correction applied to their source counts, where the GLEAM-X completeness estimations exhibit a decrease in this range (Ross et al. 2024). Additionally, the under-predicated flux densities in GLEAM-X for fainter sources as discussed in Sections 3.2.2 and 5.3 will have additional effects on the reported source counts at lower flux densities.

For the comparisons with the 144 MHz source counts by Shimwell et al. (2026), we see good agreeance for GAMA9 with a slight deviation at the bright end and good agreement with GAMA23 with a small deviation at flux densities <10 mJy/beam where we approach the observing limit of GAMA9. The comparisons with the ∼150 MHz source counts, exhibit agreement with Mandal et al. (2021) down to ∼25 mJy. Williams et al. (2013) shows increasing scatter around these flux density levels, but we observe agreeance with their higher calculations. Below this point we see a deviation in the counts where several factors are likely at influence. Cosmic variance due to the smaller survey area may be a contributing factor. Additionally, the source counts are based on surveys with a higher resolution that likely resolves some sources into multiple fainter sources instead of a single brighter source observed in MIDAS. Finally, the MIDAS source catalogues were produced with `AEGEAN` where we classified each 2D Gaussian component as a radio source, while Williams et al. (2013) and Mandal et al. (2021) utilise PYthon Blob Detector and Source Finder[q] (PyBDSF) that groups 2D Gaussians connected via continuous emission into a single source. Mandal et al. (2021) then performed additional steps to deblend physically distinct radio sources that were classified as a single source and consolidate sources with multiple separate radio components (e.g. radio lobes) into a single source. These variations in source classification will result in a discrepancy in source counts between surveys.

The resulting source counts may be adequately described by third-degree polynomials. Fitting the polynomial

$$\log_{10}\left(S^{2.5}\frac{dN}{dS}\right) = a\log_{10}(S)^3 + b\log_{10}(S)^2 + c\log_{10}(S) + d \quad (9)$$

to the GAMA9 and GAMA23 counts, where S is the 215.68 MHz flux density measured in Jy for the respective fields, results with the constants outlined in Table 11.

5.7. Spectral properties of the sample

Sources within the GAMA23 MIDAS catalogue were matched with the 887.5 MHz deep field source catalogue produced from the ASKAP EMU Early Science project by Gürkan et al. (2022) and

[q] https://github.com/sabourke/pybdsf.

https://doi.org/10.1017/pasa.2026.10245 Published online by Cambridge University Press

Table 11. The resulting constants for a third-degree polynomial fitted to the GAMA9 and GAMA23 source counts.

Field	a	b	c	d
GAMA9	-0.0288 ± 0.0160	-0.256 ± 0.040	0.267 ± 0.032	3.33 ± 0.02
GAMA23	-0.0537 ± 0.0119	-0.283 ± 0.030	0.300 ± 0.024	3.36 ± 0.02

the GAMA spectroscopic redshift catalogue (Driver et al. 2022). A maximum separation distance of 1′ was used for the source matching, resulting in a total of 12 640 sources cross-matched to the EMU catalogue and 5 861 spectroscopic redshifts identified. We detected 846 sources in the GAMA23 MIDAS catalogue within the area imaged by EMU that did not have a corresponding source within 1′ in the EMU catalogue. Most of these non-detected sources were due to the different source finding methods. Gürkan et al. (2022) used PyBSDF for their source finding and then visually inspected and consolidated radio galaxies with clearly distinct jets and cores into a single source. Our use of AEGEAN attempts to fit 2D Gaussians to the sources, resulting in the core and jets or multiple sections of a complex source being defined as separate sources.

Furthermore, many of the sources not detected in EMU are on the edge of the EMU mosaic in high RMS areas, including some sources on the image border, causing them to be cropped. However, there were 60 sources located in the lower RMS areas near the centre of the EMU mosaic that were not detected suggesting spectra with steep negative spectral indices, typical of older emission from remnant radio galaxies or galaxy cluster relics.

From the sources detected in both catalogues, we calculated their spectral indices and identified 35 sources with a spectral index $\alpha_{888}^{216} < -2$ and 5 sources with a spectral index $\alpha_{888}^{216} > 0.7$. These are atypical of standard synchrotron emission from radio galaxies and could point towards interesting physics or objects. In Figure 12 we present the spectral distribution for the point sources calculated between the flux densities in the GAMA23 MIDAS survey at 215.68 MHz and the EMU survey at 887.5 MHz along with several of the non-detected sources. For the non-detected sources, the upper limit for the spectral index was calculated from EMU's 5σ source detection limit 0.19 mJy, aligning well with the slope observed for the detected sources in the negative spectral index region. The matched sources were filtered based on the EMU catalogue to those reported as a point source, while non-detected sources were selected from the GAMA23 MIDAS catalogue for a region 8° by 4° at the centre of the GAMA23 field to ensure the corresponding area within the EMU image had a low RMS. To lower the likelihood of false detections, we filtered out detected sources within 3′ of sources with an integrated flux density > 0.8 Jy where noise can exceed 5σ. To filter out sources that may be classified differently between the catalogues, the pixel value at each source location was measured, along with the mean of the pixel values for a 20 pixel by 20 pixel region around it. We then selected the sources where these values were below the 5σ EMU detection threshold. A brief visual inspection of the 60 sources was performed to verify they were likely genuine.

Here, we provide a closer inspection for 3 example sources with extreme negative and positive spectral indices detailed in Table 12. From the 35 sources with a spectral index $\alpha_{888}^{216} < -2$, we randomly selected a source that was detected in both surveys (MIDAS J225807-321424) along with one of the brightest sources in MIDAS that was not detected in EMU (MIDAS J225817-320052).

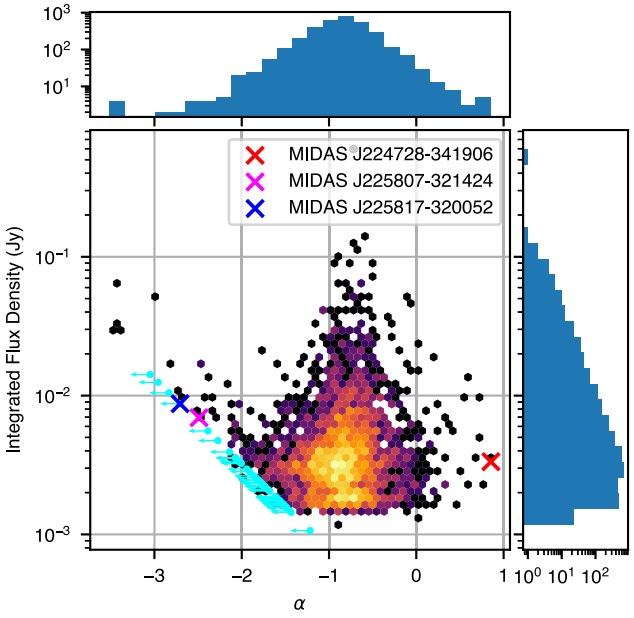
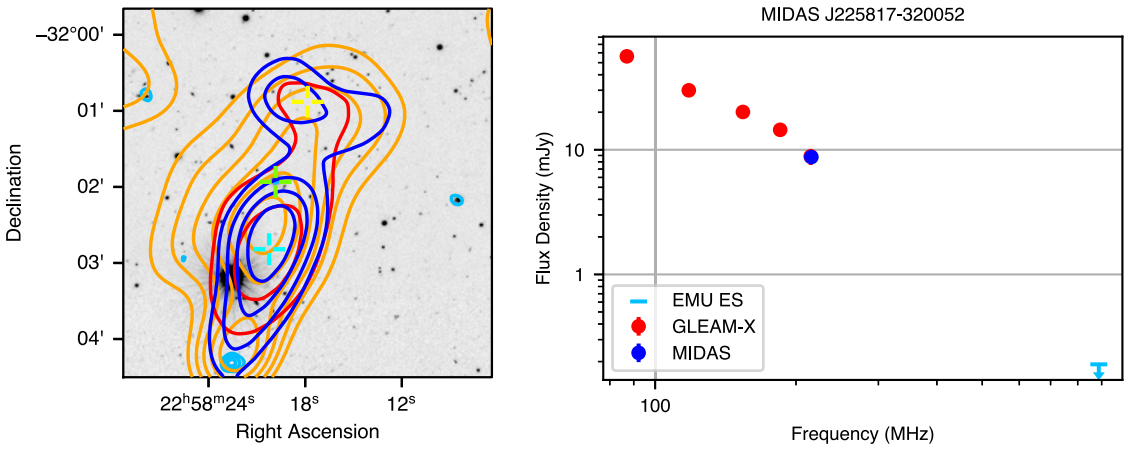


Figure 12. The integrated flux density at 215.68 MHz as a function of the spectral indices α between 215.68 and 887.5 MHz for sources in the GAMA23 MIDAS catalogue matched to a source within 1′ of the GAMA23 EMU catalogue (Gürkan et al. 2022). The sources were filtered to unresolved sources along with a selection of sources not detected in EMU as described in the text. The cyan markers are the upper-limits on the spectral index for the selection of sources not detected within EMU. The crosses represent 3 examples of steep spectrum sources, selected to highlight the potential of the catalogue. Here we select one negative spectrum source that is detected in both MIDAS and EMU, one negative spectrum source not detected in EMU and one positive spectrum source.

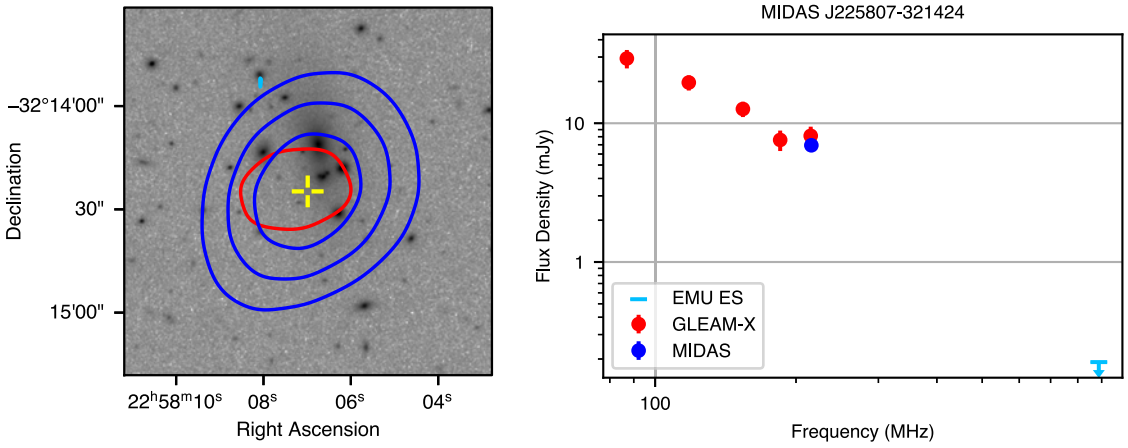
From the 5 sources with a spectral index $\alpha_{888}^{216} > 0.7$, we selected the source with the highest spectral index, MIDAS J224728-341906. These sources are detailed in Figure 13 using optical data overlaid with the observed radio contours. The optical data is Z-band imaging from the Visible and Infrared Survey Telescope for Astronomy (VISTA) Kilo-degree Infrared Galaxy (VIKING) survey (Findlay et al. 2012) and the Dark Energy Spectroscopic Instrument Legacy Imaging Surveys (Dey et al. 2019), while the radio contours are from the MIDAS mosaics, GLEAM-X, EMU Early Science and VLASS.

MIDAS J225817-320052 with an integrated flux density of 8.74 ± 0.34 mJy measured in MIDAS was not detected within the EMU mosaic, but is observed in GLEAM-X (GLEAM-X J225817.9-320049) with an integrated flux density of 12.08 ± 1.74 mJy in the wideband mosaic centred at 200 MHz. Although no source was detected at this source location within the EMU mosaic, diffuse radio emission is observed that is below the EMU detection threshold. The source in MIDAS is likely a radio lobe where a potential host (EMUJ225819.9-320156, GAMAJ225819.84-320154.0) is observed in the EMU mosaic south-southeast to the radio emission with a spectroscopic redshift of $z = 0.317$. Additionally, a second brighter source, which is likely the opposing lobe, is observed in MIDAS and GLEAM-X on the opposite side. When convolving EMU to the same beam size as MIDAS, only a large single source, which encompasses the area of the host and lobes, is observed with a peak between the potential host and the southern lobe; this is likely due to the uneven contribution of the radio lobes. The EMU source detected south of the lower lobe appears to be an unrelated background galaxy.

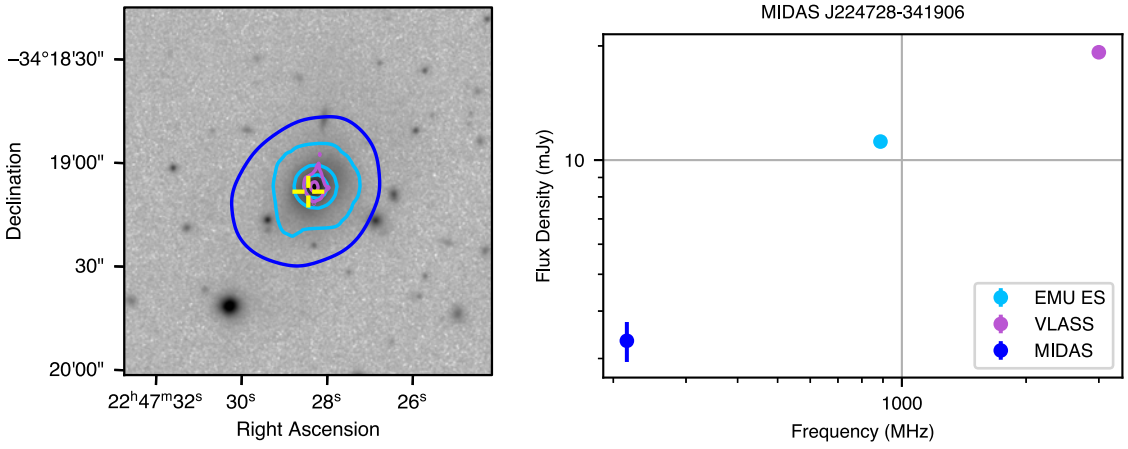
https://doi.org/10.1017/pasa.2026.10245 Published online by Cambridge University Press



(a) MIDAS J225817-320052 with diffuse emission below the detection threshold in EMU. The source is likely one lobe of an asymmetric radio galaxy. The yellow crosshair is the MIDAS lobe not detected in EMU, the green crosshair is the potential host and the cyan crosshair is the the second lobe. A foreground unrelated star is observed in the bottom-left of the optical image.



(b) MIDAS J225807-321424, likely diffuse emission from the galaxy cluster GAMAJ225806.74-321411.1 with a point source EMU detection to the top-left just above the 5σ MIDAS contour.



(c) MIDAS J224728-341906, a galaxy with a steep positive spectrum at the low-radio frequencies detected slightly above the 5σ MIDAS detection threshold. It is very bright at 887.5 MHz in EMU but is below the detection threshold of GLEAM-X (Ross et al. 2024).

Figure 13. Postage stamp radio overlay images of three rare, interesting sources from the GAMA23 field along with their SEDs. The optical background data is *Z*-band imaging from VISTA. The contours are GAMA23 MIDAS 215.68 MHz (blue), EMU Early Science 887.5 MHz (sky blue), EMU Early Science 887.5 MHz convolved to the MIDAS resolution (orange) as described in § 5.1, GLEAM-X wideband (170-231 MHz, red) and VLASS 3 GHz (purple). The contours start at the reported 5σ threshold with 50 even increments in log-space to 40σ for MIDAS J225817-320052 and MIDAS J225807-321424 and three even increments for MIDAS J224728-341906. The yellow crosshairs mark the locations of the sources detected in MIDAS. The SEDs contain the measured integrated flux densities for the sources in each respective survey with the exception of the EMUES values for MIDAS J225818-32005 and MIDAS J225806-32142; as these sources were not detected, we have used their 5σ detection threshold for the upper limit.

https://doi.org/10.1017/pasa.2026.10245 Published online by Cambridge University Press

Table 12. Details for the three example sources selected from the MIDAS catalogue with extreme spectral indices where 35 sources were identified with a spectral index $\alpha_{888}^{216} < -2$ and 5 sources with a spectral index $\alpha_{888}^{216} > 0.7$. We selected a random source from the negative spectrum population that was detected in both MIDAS and EMU along with a source with one of the steepest negative spectrum that was not detected in EMU. From the positive spectrum population, we selected the source with the highest positive spectral index.

	MIDAS J225817-320052	MIDAS J225807-321424	MIDAS J224728-341906
RA (deg)	344.57462	344.52914	341.86905
Dec (deg)	−32.01452	−32.24020	−34.31851
α_{888}^{216}	< -2.7	< -2.5	0.85 ± 0.07
Int flux density (mJy)	8.74	6.94	3.34
Peak flux density (mJy/beam)	3.53	6.14	3.19
Local RMS (mJy/beam)	0.338	0.344	0.348
GLEAM-X source	GLEAM-X J225817.9-320049	GLEAM-X J225807.1-321424	–
EMU source	–	EMUJ225808.0-321353 (Mismatch)	EMUJ224728.4-341905
GAMA source	–	GAMAJ225806.74-321411.1	GAMAJ224728.42-341904.8
Redshift	0.317 (Host)	0.198	0.120

Asymmetric double radio sources are unusual. Jet powers are likely similar from either pole of a black hole so the differing morphology is most likely due to environmental affects. For example, a denser medium on the southern side could keep a jet collimated longer meaning that we still see a hotspot. Or the southern lobe could be angled away from us so we are seeing it at a younger age than the northern lobe (which would be angled towards us).

MIDAS J225807-321424, randomly selected from the $\alpha_{888}^{216} < -2$ population with an integrated flux density of 6.94 ± 0.34 mJy in MIDAS matched to EMUJ225808.0-321353 with an integrated flux density of 0.205 ± 0.034 mJy resulting in a spectral index of $\alpha_{888}^{216} = -2.5 \pm 0.1$. The MIDAS source position corresponds to the galaxy cluster GAMAJ225806.74-321411.1 (Robotham et al. 2011) and has a reported spectroscopic redshift of $z = 0.198$ (Driver et al. 2022). This source is also detected in the GLEAM-X wideband mosaic centred at 200 MHz with an integrated flux density of 8.37 ± 0.97 mJy. The detection within the 887.5 MHz EMU image occurs north-northeast of the cluster, which appears to be a separate source to the MIDAS detection and therefore is a mismatch resulting in an incorrect spectral index. Within the 215.68 MHz GAMA23 MIDAS mosaic, the detection occurs near the centre of the cluster, at this location in the convolved EMU mosaic, the radio emission is below the 5σ detection threshold of 0.190 mJy. Setting an upper limit for the source within EMU as 5σ, we estimate a spectral index of <-2.5

From the sources with positive spectral indices $\alpha_{888}^{216} > 0.7$, we selected MIDAS J224728-341906 which had the highest spectral index in the sample with $\alpha_{888}^{216} = 0.85 \pm 0.07$. It was observed with an integrated flux density of 3.34 ± 0.35 mJy at 215.68 MHz within the GAMA23 MIDAS mosaic which is too faint to be detected in GLEAM-X. Within EMU at 887.5 MHz, it was detected with an integrated flux density of 11.2 ± 0.1 mJy and was detected in VLASS at 3 GHz with an integrated flux density of 19.24 ± 0.13 mJy (Gordon et al. 2021). The source position corresponds to a known galaxy with a spectroscopic redshift of $z = 0.120$ (Driver et al. 2022), previously observed in radio (Wright et al. 1996; Mauch et al. 2013; Gordon et al. 2021), infrared (Cutri et al. 2013), optical (Maddox et al. 1990) and ultraviolet (Bianchi et al. 2011). The low-frequency MIDAS measurement may be used to help constrain the spectral peak and fit for this source. This source has no reported evidence of variability, so is likely a very young high-frequency peaker. Young radio galaxies peak due to synchrotron self-absorption and that peak moves to lower frequencies as the radio source expands. Future work could model the radio spectra to help determine the mechanism causing the the turn-over.

6. Conclusion

In this paper, we have presented deep field mosaics produced from the MIDAS survey, with an angular resolution of $\sim 60''$, covering the GAMA9 and GAMA23 regions that were observed by the MWA at a central frequency 215.68 MHz with a bandwidth of 30.72 MHz. The GAMA9 MIDAS deep field image covers an area $\sim 1\,250$ deg^2 centred at RA $+135°$, Dec $+0.5°$. A total of 1 282 observations were mosaicked, resulting in 42.7 h of integration time achieving an RMS of 0.923 ± 0.003 mJy/beam within the GAMA9 region, a depth comparable to RACS and VLASS. The GAMA23 MIDAS deep field image achieved an RMS of 0.331 ± 0.001 mJy/beam within the GAMA23 region from 56.7 h of integration time (1 701 observations) which we believe to be the deepest image produced from the MWA to date. This mosaic covered a ~ 850 deg^2 area centred at RA $+345°$, Dec $-32.5°$. The low noise achieved at this frequency enables new insight into this field, offering low-frequency radio data to depths comparable to the higher frequency expectant GLASS release and close to the early EMU release.

The MIDAS deep field data complements the wide-field GLEAM-X survey, offering a 2–5× improvement in sensitivity for a narrow band centred on 215.68 MHz in the selected fields of interest. The GAMA23 mosaic approaches the limits of deep field imaging with the MWA, where the asymptotic nature of Figure 3 suggests the need for longer baselines or additional imaging steps, such as self-calibration or joint deconvolution (Mantovanini et al. 2025), to achieve more significant improvements. The GAMA9 mosaic illustrates the challenges of performing deep surveys with wide-field radio telescopes when there are bright sources within the instrumental response. This highlights the importance in the selection of deep fields for future observations with wide-field radio interferometer telescopes such as the MWA and the SKAO's Low telescope.

https://doi.org/10.1017/pasa.2026.10245 Published online by Cambridge University Press

The observation processing required to create these mosaics was completed with `DIP`, a pipeline we developed for deep imaging of MWA data based on the data reduction methods of GLEAM-X (Hurley-Walker et al. 2022). The pipeline has been optimised to minimise the thermal and sidelobe noise while implementing automation that enables the processing of thousands of observations with minimal user interaction.

From the deep field mosaics, we generated source catalogues adding valuable low-frequency radio data to an existing wealth of shorter wavelength information. From the GAMA9 MIDAS survey, we detected 53 419 sources with a source density of 70.42 sources/deg^2 (52.0 beams per source). The catalogue resulting from the GAMA23 MIDAS survey resulted in 80 407 sources with a source density of 140.28 sources/deg^2 (32.4 beams per source) which approaches the classical confusion limit. Evaluating the accuracy of the source catalogues, we have demonstrated agreement in the astrometry with NVSS and SUMSS along with RACS-high. Additionally, we demonstrate good agreement in flux density scaling with our reference catalogue GLEAM. A small systematic flux density scale difference between MIDAS and GLEAM-X DRII as a function of SNR is observed. We surmise this is likely due to the 3σ `auto-mask` chosen for `CLEAN`ing in GLEAM-X resulting in a large number of noise peaks being deconvolved and removing flux from true sources.

We have presented the normalised differential source counts calculated from the 215.68 MHz catalogues. The source counts exhibited good agreement with the 200 MHz counts by Franzen et al. (2019), but a deviation below ∼40 mJy with the counts derived from GLEAM-X by Venville et al. (2024). We attribute this to the lack of a completeness correction applied to their source counts. At ∼150 MHz, we observe agreement with Mandal et al. (2021) and the upper estimations of Mandal et al. (2021) from their brightest measurements to ∼25 mJy. At lower flux density limits, we measure higher source counts; this may be due to the difference in resolution and sensitivity of the surveys along with the different source finding methods implemented.

We matched the GAMA23 MIDAS source catalogue to the 887.5 MHz GAMA23 source catalogues produced by Gürkan et al. (2022) and identified 35 sources with a spectral index $\alpha_{888}^{216} < -2$ and 5 sources with a spectral index $\alpha_{888}^{216} > 0.7$. We selected a small sample of these sources from which we observed emission from a galaxy cluster, diffuse emissions, and a galaxy not previously detected at low frequencies.

The deep field images and catalogues offer further insight into the low-frequency emission for the regions. A prepublished MIDAS mosaic of the GAMA23 field produced from this work was utilised by Ighina et al. (2024) to determine the 216 MHz upper limit for a z∼6.5 radio-loud quasi stellar object (QSO).

In future work, we will combine our source catalogues with the plethora of data available for the GAMA9 and GAMA23 regions in an attempt to produce accurate radio luminosity function (RLF)s. The low-frequency RLFs will be important tools for the future study of galaxy evolution.

Acknowledgements. SP thanks Kat Ross for the assistance provided to understand the GLEAM-X results.

This research is supported by an Australian Government Research Training Program (RTP) Scholarship. N.H.-W. is the recipient of an Australian Research Council Future Fellowship (project number FT190100231).

This scientific work uses data obtained from Inyarrimanha Ilgari Bundara, the CSIRO Murchison Radio-astronomy Observatory. We acknowledge the Wajarri Yamaji People as the Traditional Owners and Native Title Holders of the observatory site. Support for the operation of the MWA is provided by the Australian Government (NCRIS), under a contract to Curtin University administered by Astronomy Australia Limited. We acknowledge the Pawsey Supercomputing Centre which is supported by the Western Australian and Australian Governments.

This research made use of hips2fits,[r] a service provided by CDS; the NASA/IPAC Extragalactic Database (NED), which is operated by the Jet Propulsion Laboratory, California Institute of Technology, under contract with the National Aeronautics and Space Administration; NASA's Astrophysics Data System and the VizieR catalogue access tool, CDS, Strasbourg, France.

A range of `python` packages were used for this work including `pandas` (McKinney 2010, 2011); `wcsaxes`, an open-source plotting library for Python hosted at https://wcsaxes.readthedocs.io/en/latest/; `Astropy`, a community-developed core Python package for Astronomy (Astropy Collaboration et al. 2013, 2018); `SciPy` (Virtanen et al. 2020); matplotlib, a Python library for publication quality graphics (Hunter 2007) and `NumPy` (Harris et al. 2020).

This research made use of `ds9`, a tool for data visualisation supported by the Chandra X-ray Science Center (CXC) and the High Energy Astrophysics Science Archive Center (HEASARC) with support from the JWST Mission office at the Space Telescope Science Institute for 3D visualisation and `TOPCAT`, an interactive graphical viewer and editor for tabular data (Taylor 2005). The acknowledgements were compiled with help from the Astronomy Acknowledgement Generator.

This paper includes data that has been provided by AAO Data Central (datacentral.org.au).

Some of the results in this paper have been derived using the HEALPix (Gorski et al. 2005) package.

Data availability statement. The Deep Imaging Pipeline is available from https://github.com/sjpaterson/dip. The deep field mosaics, RMS maps, PSF maps, and catalogues produced in this work for the GAMA9 and GAMA23 regions are available to download from the Data Central PASA Datastore (https://doi.org/10.57891/z19a-2n41).

References

Arras, P., Reinecke, M., Westermann, R., & Enßlin, T. A. 2021, A&A, 646, A58
Astropy Collaboration, et al. 2018, 156, 123
Astropy Collaboration, et al. 2013, 558, A33
Beardsley, A. P., et al. 2019, PASA, 36, e050
Bertin, E., Mellier, Y., Radovich, M., Missonnier, G., Didelon, P., & Morin, B. 2002, 281, 228. https://ui.adsabs.harvard.edu/abs/2002ASPC..281..228B (Accessed October 11, 2024)
Beswick, R. J., et al. 2015, in Proceedings of Advancing Astrophysics with the Square Kilometre Array — PoS(AASKA14) (Giardini Naxos, Italy: Sissa Medialab), 070. https://doi.org/10.22323/1.215.0070 (Accessed October 4, 2024)
Bianchi, L., Herald, J., Efremova, B., Girardi, L., Zabot, A., Marigo, P., Conti, A., & Shiao, B. 2011, Ap&SS, 335, 161
Bock, D. C.-J., Large, M. I., & Sadler, E. M. 1999, AJ, 117, 1578
Condon, J. J. 1974, ApJ, 188, 279
Condon, J. J., Cotton, W. D., Greisen, E. W., Yin, Q. F., Perley, R. A., Taylor, G. B., & Broderick, J. J. 1998, AJ, 115, 1693
Cutri, R. M., et al. 2013, Technical report (Accessed October 18, 2024)
DeBoer, D. R., et al. 2009, Proc. IEEE, 97, 1507
Dey, A., et al. 2019, AJ, 157, 168
Di Tommaso, P., Chatzou, M., Floden, E. W., Barja, P. P., Palumbo, E., & Notredame, C. 2017, NBT, 35, 316
Driver, S. P., et al. 2022, MNRAS, 513, 439
Driver, S. P., et al. 2009, A&G, 50, 5.12
Duchesne, S. W., Johnston-Hollitt, M., Zhu, Z., Wayth, R. B., & Line, J. L. B. 2020, PASA, 37, e037

[r] https://alasky.cds.unistra.fr/hips-image-services/hips2fits.

Duchesne, S. W., et al. 2025a, PASA, 42, e158
Duchesne, S. W., et al. 2025b, PASA, 42, e038
Duchesne, S. W., et al. 2023, PASA, 40, e034
Eddington, A. S. 1913, MNRAS, 73, 359
Findlay, J. R., Sutherland, W. J., Venemans, B. P., Reylé, C., Robin, A. C., Bonfield, D. G., Bruce, V. A., & Jarvis, M. J. 2012, MNRAS, 419, 3354
Franzen, T. M. O., et al. 2016, MNRAS, 459, 3314
Franzen, T. M. O., et al. 2021, PASA, 38, e041
Franzen, T. M. O., Vernstrom, T., Jackson, C. A., Hurley-Walker, N., Ekers, R. D., Heald, G., Seymour, N., & White, S. V. 2019, PASA, 36, e004
Gehrels, N. 1986, ApJ, 303, 336
George, L. T., et al. 2015, MNRAS, 451, 4207
George, L. T., et al. 2017, MNRAS, 467, 936. https://doi.org/10.1093/mnras/stx155
Gordon, Y. A., et al. 2021, https://doi.org/10.26093/CDS/VIZIER.22550030 (Accessed January 17, 2025)
Gorski, K. M., Hivon, E., Banday, A. J., Wandelt, B. D., Hansen, F. K., Reinecke, M., & Bartelmann, M. 2005, ApJ, 622, 759
Gupta, Y., et al. 2017, CSci, 113, 707
Gürkan, G., et al. 2022, MNRAS, 512, 6104
Hancock, P. J., Murphy, T., Gaensler, B. M., Hopkins, A., & Curran, J. R. 2012, MNRAS, 422, 1812
Hancock, P. J., Trott, C. M., & Hurley-Walker, N. 2018, PASA, 35, e011
Harris, C. R., et al. 2020, Natur, 585, 357
Harris, F. J. 1978, Proc. IEEE, 66, 51
Heesen, V., et al. 2019, A&A, 622, A8
Hogg, D. W., & Turner, E. L. 1998, PASP, 110, 727
Hopkins, A. M., et al. 2025, https://ui.adsabs.harvard.edu/link_gateway/2025PASA...42...71H/ (Accessed July 10, 2025)
Hotan, A. W., et al. 2021, PASA, 38, e009
Hunter, J. D. 2007, CSE, 9, 90
Hurley-Walker, N., et al. 2017, MNRAS, 464, 1146
Hurley-Walker, N., et al. 2022, PASA, 39, e035
Hurley-Walker, N., et al. 2019, PASA, 36, e047
Hurley-Walker, N., & Hancock, P. J. 2018, A&C, 25, 94
Ighina, L., et al. 2024, A&A, 687, A242
Johnston, S., et al. 2007, PASA, 24, 174
Kellermann, K. I. 1964, ApJ, 140, 969
Lacy, M., et al. 2020, PASP, 132, 035001
Leahy, D. A., et al. 2019, PASA, 36, e024
Liske, J., et al. 2015, MNRAS, 452, 2087
Maddox, S. J., Sutherland, W. J., Efstathiou, G., & Loveday, J. 1990, MNRAS, 243, 692
Mandal, S., et al. 2021, A&A, 648, A5
Mantovanini, S., Becker, W., Khokhriakova, A., Hurley-Walker, N., Anderson, G. E., & Nicastro, L. 2024, A&A, 690, A278
Mantovanini, S., Hurley-Walker, N., Ross, K., Duchesne, S., Anderson, G., & Galvin, T. J. 2025, PASA, 42, e137
Mauch, T., Murphy, T., Buttery, H. J., Curran, J., Hunstead, R. W., Piestrzynski, B., Robertson, J. G., & Sadler, E. M. 2003, MNRAS, 342, 1117
Mauch, T., Murphy, T., Buttery, H. J., Curran, J., Hunstead, R. W., Piestrzynski, B., Robertson, J. G., & Sadler, E. M. 2013, VizieR Online Data Catalog, 8081, VIII/81B (Accessed October 18, 2024).
McConnell, D., et al. 2020, PASA, 37, e048
McKinney, W. 2010, in Proceedings of the 9th Python in Science Conference, Austin, TX, Vol. 445, 51
McKinney, W. 2011, Python for High Performance and Scientific Computing, 14.
Morgan, J. S., Chhetri, R., & Ekers, R. 2022, PASA, 39, e063
Morgan, J., & Galvin, T. 2021, *Johnsmorgan/mwa_pb_lookup: Version 1.0.* Zenodo. https://doi.org/10.5281/zenodo.5083990
Moss, V., Hotan, A., Whiting, M., & Huynh, M. 2020, http://hdl.handle.net/102.100.100/348393?index=1
Murphy, T., Mauch, T., Green, A., Hunstead, R. W., Piestrzynska, B., Kels, A. P., & Sztajer, P. 2007, MNRAS, 382, 382
Norris, R. P., et al. 2021, PASA, 38, e046
Offringa, A. R., & Smirnov, O. 2017, MNRAS, 471, 301
Offringa, A. R., et al. 2014, MNRAS, 444, 606
Offringa, A. R., et al. 2016, MNRAS, 458, 1057
Quici, B., et al. 2021, PASA, 38, e008
Robotham, A. S. G., et al. 2011, MNRAS, 416, 2640
Ross, K., et al. 2024, PASA, 41, e054
Sault, R. J., Staveley-Smith, L., & Brouw, W. N. 1996, A&AS, 120, 375
Seymour, N., et al. 2020, PASA, 37, e013
Shimwell, T. W., et al. 2022, A&A, 659, A1
Shimwell, T. W., et al. 2026, A&A, 707, A198
Shimwell, T. W., et al. 2017, A&A, 598, A104
Shimwell, T. W., et al. 2019, A&A, 622, A1
Sokolowski, M., et al. 2017, PASA, 34, e062
Taylor, M. B. 2005, in Astronomical Data Analysis Software and Systems XIV, Vol. 347, Astronomical Society of the Pacific Conference Series ed. P. Shopbell, M. Britton, & R. Ebert, 29
Thorne, J. E., et al. 2021, MNRAS, 509, 4940
Tingay, S. J., et al. 2013, PASA, 30, e007
Van Der Tol, S., Veenboer, B., & Offringa, A. R. 2018, A&A, 616, A27
Van Haarlem, M. P., et al. 2013, A&A, 556, A2
Venville, B., Parkinson, D., Hurley-Walker, N., Galvin, T. J., & Ross, K. 2024, PASA, 41, e070
Virtanen, P., et al. 2020, NM, 17, 261
Wayth, R. B., et al. 2015, PASA, 32, e025
Wayth, R. B., et al. 2018, PASA, 35, e033
Williams, W. L., Intema, H. T., & Röttgering, H. J. A. 2013, A&A, 549, A55
Williams, W. L., et al. 2016, MNRAS, 460, 2385
Wright, A. E., Griffith, M. R., Hunt, A. J., Troup, E., Burke, B. F., & Ekers, R. D. 1996, ApJS, 103, 145
Ye, H., Gull, S. F., Tan, S. M., & Nikolic, B. 2022, MNRAS, 510, 4110

https://doi.org/10.1017/pasa.2026.10245 Published online by Cambridge University Press

Appendix A. Source masking for noise analysis

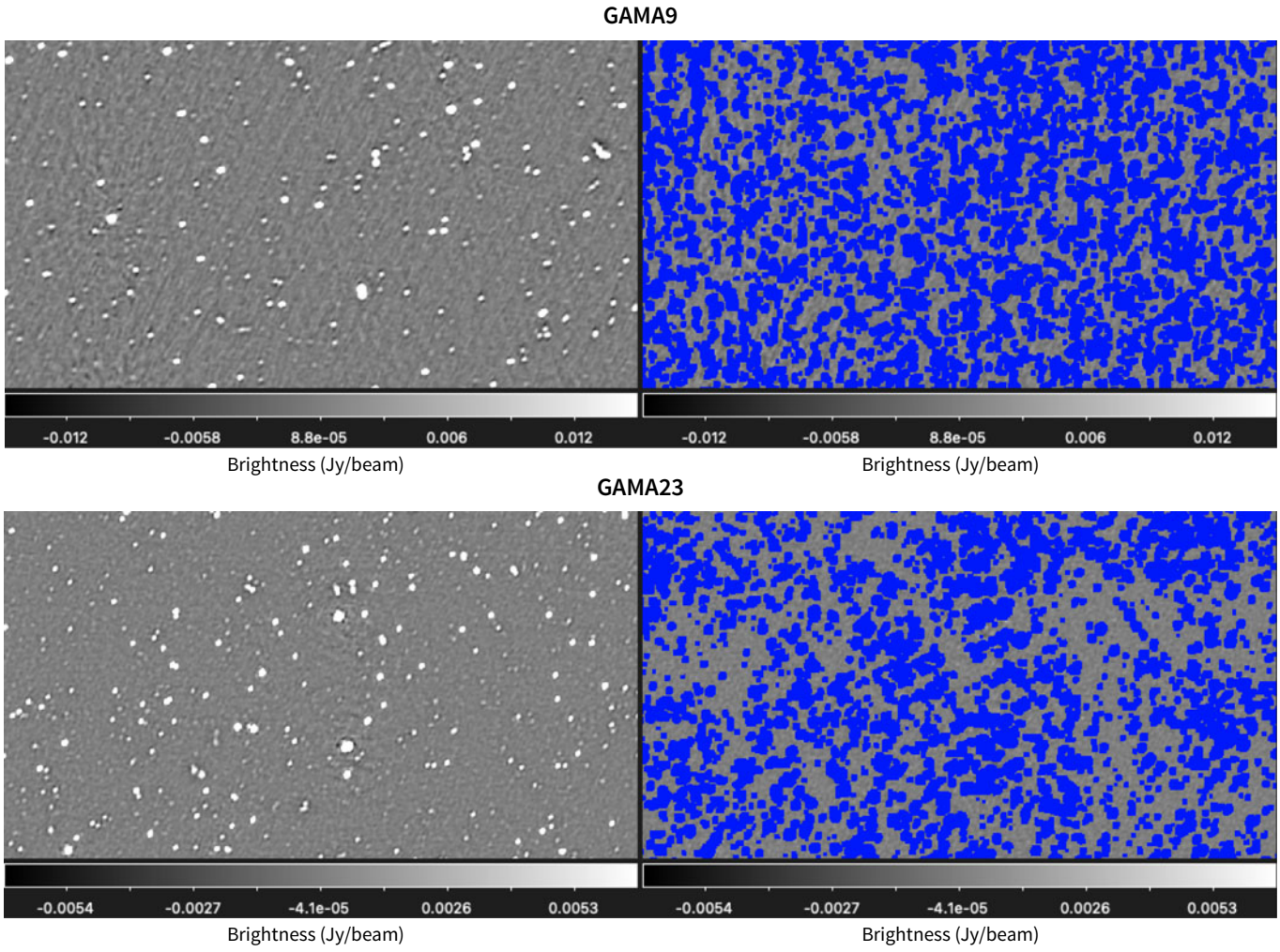


Figure A1. An example of the source masking used for the noise analysis in Section 5.1. Each cutout covers a 3.8 deg^2 area with the top panels cutout from the MIDAS GAMA9 mosaic and the bottom panels from the MIDAS GAMA23 mosaic. The left-hand panels are cutouts from the mosaic while the right-hand panels are the cutouts with the masking (blue) overlayed.

https://doi.org/10.1017/pasa.2026.10245 Published online by Cambridge University Press

Appendix B. Ionospheric 'blur' maps

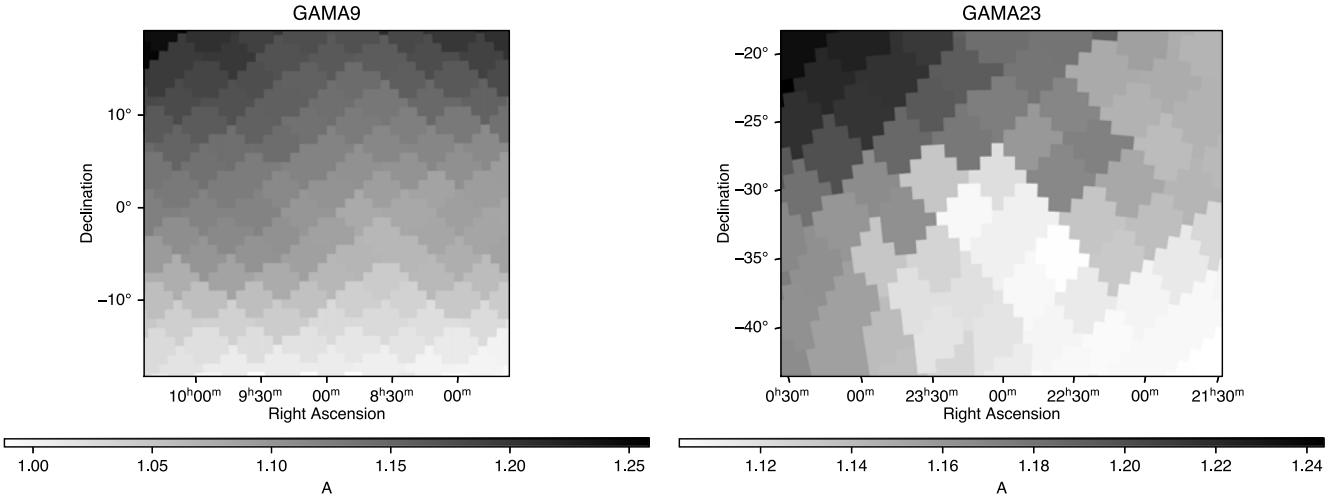


Figure B1. The resulting blurring factors (A) calculated in Section 4.4 applied to each MIDAS mosaic to correct the underestimated measured peak flux densities due to ionospheric blurring. Each pixel corresponds to approximately one square-degree.

Appendix C. Source catalogue column headings

Table C1. The column names, units and description for the 215.68 MHz MIDAS GAMA source catalogues. The naming follows the coordinate-based naming convention of the International Astronomical Union. The remainder of the columns are the results output by `AEGEAN`.

Number	Name	Unit	Description
1	Name	hh:mm:ss+dd:mm:ss	International Astronomical Union name
2	background	Jy/beam	Background flux density level
3	local_rms	Jy/beam	Local RMS
4	ra_str	hh:mm:ss	Right ascension
5	dec_str	hh:mm:ss	Declination
6	ra	degrees	Right ascension
7	err_ra	degrees	Uncertainty on the right ascension
8	dec	degrees	Declination
9	err_dec	degrees	Uncertaincty on the declination
10	peak_flux	Jy/beam	Peak flux density
11	err_peak_flux	Jy/beam	Uncertainty for the peak flux density
12	int_flux	Jy	Integrated flux density
13	err_int_flux	Jy	Uncertainty for the integrated flux density
14	a	arcsec	Fitted major axis of the source
15	err_a	arcsec	Uncertainty for the major axis of the source
16	b	arcsec	Fitted minor axis of the source
17	err_b	arcsec	Uncertainty for the minor axis of the source
18	pa	degrees	Fitted position angle of the source
19	err_pa	degrees	Uncertainty for the position angle of the source
20	residual_mean	Jy/beam	Mean of the residual after source fitting
21	residual_std	Jy/beam	Standard deviation of residual after source fitting
22	psf_a	arcsec	Major axis of the PSF at location of source
23	psf_b	arcsec	Minor axis of the PSF at location of source
24	psf_pa	degrees	Position angle of the PSF at location of source
25	reliability	flag	A 'low' flag for sources within close proximity to a bright source

https://doi.org/10.1017/pasa.2026.10245 Published online by Cambridge University Press